SPECIAL
Global Precipitation Measurement (GPM)
COLLECTION

Global Assessment of the Capability of Satellite Precipitation Products to Retrieve Landslide-Triggering Extreme Rainfall Events

ODIN MARC,[a] ROMULO A. JUCÁ OLIVEIRA,[b] MARIELLE GOSSET,[a] ROBERT EMBERSON,[c,d,e] AND JEAN-PHILIPPE MALET[f]

[a] *Géosciences Environnement Toulouse, CNRS/IRD/CNES/UPS, Observatoire Midi-Pyrénées, Toulouse, France*
[b] *Laboratoire d'Etudes en Géophysique et Océanographie Spatiales, Université de Toulouse III/CNRS/CNES/IRD, Observatoire Midi-Pyrénées, Toulouse, France*
[c] *Hydrological Sciences Laboratory, NASA Goddard Space Flight Center, Greenbelt, Maryland*
[d] *Universities Space Research Association, Columbia, Maryland*
[e] *NASA Goddard Earth Sciences Technology and Research, Columbia, Maryland*
[f] *Institut Terre et Environnement de Strasbourg, CNRS/UMR7063, EOST/Université de Strasbourg, Strasbourg, France*

(Manuscript received 12 November 2021, in final form 8 May 2022)

ABSTRACT: Rainfall-induced landsliding is a global and systemic hazard that is likely to increase with the projections of increased frequency of extreme precipitation with current climate change. However, our ability to understand and mitigate landslide risk is strongly limited by the availability of relevant rainfall measurements in many landslide prone areas. In the last decade, global satellite multisensor precipitation products (SMPP) have been proposed as a solution, but very few studies have assessed their ability to adequately characterize rainfall events triggering landsliding. Here, we address this issue by testing the rainfall pattern retrieved by two SMPPs (IMERG and GSMaP) and one hybrid product [Multi-Source Weighted-Ensemble Precipitation (MSWEP)] against a large, global database of 20 comprehensive landslide inventories associated with well-identified storm events. We found that, after converting total rainfall amounts to an anomaly relative to the 10-yr return rainfall R^*, the three products do retrieve the largest anomaly (of the last 20 years) during the major landslide event for many cases. However, the degree of spatial collocation of R^* and landsliding varies from case to case and across products, and we often retrieved $R^* > 1$ in years without reported landsliding. In addition, the few (four) landslide events caused by short and localized storms are most often undetected. We also show that, in at least five cases, the SMPP's spatial pattern of rainfall anomaly matches landsliding less well than does ground-based radar rainfall pattern or lightning maps, underlining the limited accuracy of the SMPPs. We conclude on some potential avenues to improve SMPPs' retrieval and their relation to landsliding.

SIGNIFICANCE STATEMENT: Rainfall-induced landsliding is a global hazard that is expected to increase as a result of anthropogenic climate change. Our ability to understand and mitigate this hazard is strongly limited by the lack of rainfall measurements in mountainous areas. Here, we perform the first global assessment of the potential of three high-resolution precipitation datasets, derived from satellite observations, to capture the rainfall characteristics of 20 storms that led to widespread landsliding. We find that, accounting for past extreme rainfall statistics (i.e., the rainfall returning every 10 years), most storms causing landslides are retrieved by the datasets. However, the shortest storms (i.e., ~3 h) are often undetected, and the detailed spatial pattern of extreme rainfall often appears to be distorted. Our work opens new ways to study global landslide hazard but also warns against overinterpreting rainfall derived from satellites.

KEYWORDS: Extreme events; Satellite observations; Anomalies; Atmosphere–land interaction

1. Introduction

Landsliding, broadly referring to any downslope movement of soil and rock masses, is a global hazard causing thousands of fatalities every year (Petley 2012; Froude and Petley 2018) and substantial economic losses. Together with shallow earthquakes, rainfall (intense and/or prolonged; i.e., intensity vs amounts) is the main trigger of landsliding, mainly by increasing slope pore-water pressures and reducing resistance of the soil or rock masses (Wilson and Wieczorek 1995; van Asch et al. 1999; Iverson 2000). Thus, although rainfall is often

Supplemental information related to this paper is available at the Journals Online website: https://doi.org/10.1175/EI-D-21-0022.s1.

Corresponding author: Odin Marc, odin.marc@get.omp.eu

Earth Interactions is published jointly by the American Meteorological Society, the American Geophysical Union, and the Association of American Geographers.

DOI: 10.1175/EI-D-21-0022.1

required for triggering the failure, its size, location, and timing will substantially depend on various parameters such as surface and subsurface slope geometry, material strength, and hydrological properties such as porosity and permeability (Terzaghi 1943; Iverson 2000).

Fine-scale variations of hydromechanical properties of rock mass are a strong control on landslide initiation but remain hard to constrain. This degrades the prediction of mechanistic models for rainfall-induced landsliding over regional scales (Rosso et al. 2006; Baum et al. 2010; von Ruette et al. 2014), and limits the development of landslide hazard forecasting, in contrast to other hydrometeorological hazards, such as floods (e.g., Han and Coulibaly 2017; Wu et al. 2020). Most empirical approaches have focused on developing meteorological thresholds (e.g., rainfall intensity–duration) for quantifying landslide occurrences (e.g., Caine 1980; Guzzetti et al. 2008). More recently, two new approaches have emerged. The first one aims at developing hydrometeorological thresholds (Bogaard and Greco 2018), more in line with hydrological and mechanistic considerations on landslide triggering (Mirus et al. 2018; Thomas et al. 2018). The second approach, which focuses on relating changes in landslide density with rainfall magnitude beyond the threshold, relies on the generation of large landslide inventories (Chen et al. 2013; Saito et al. 2014; Marc et al. 2018, 2019). Importantly, such approaches based on landslide populations, and not on individual landslides, require rainfall information at the catchment scale (~100 km^2) rather than at the hillslope scale (~0.1 km^2). Still, for most of these studies, limitations on rainfall and/or landslide data availability are key issues.

The proliferation of medium to high resolution (<15 m) satellite imagery (both multispectral and radar) allows researchers to detect, map and monitor landslides triggered by rainfall events in more and more settings (Marc et al. 2018; Amatya et al. 2021; Emberson et al. 2022). However, extensive in situ gauge networks (or ground-based weather radar) are lacking in most landslide-prone areas (e.g., central and Southeast Asia, Central and South America, and central Africa). Thus, for the last decade rainfall data retrieved from satellite constellation measurements have been considered as a potential alternative to study and potentially nowcast landslide hazard globally (Hong et al. 2007; Kirschbaum et al. 2009; Farahmand and AghaKouchak 2013). This approach has recently culminated into an automatic hazard awareness system, based on daily and antecedent (7 days) rainfall derived from satellite multisensor precipitation products (SMPP) and susceptibility maps derived from global maps of land cover, slope and distance to roads and faults (Kirschbaum et al. 2015; Kirschbaum and Stanley 2018; Stanley et al. 2021). The key advantages of SMPP are their global coverage, and their fair spatial and temporal resolution (typically 1 h and 0.1°). Still, many issues with the retrieved precipitation properties have been observed, including (i) difficulty in capturing orographic rainfall (AghaKouchak et al. 2011; Shige et al. 2013; Yamamoto et al. 2017), (ii) difficulty in retrieving short duration and/or very intense rainfall (Mehran and AghaKouchak 2014) or rainfall over terrain transition (e.g., coastal areas; Tan et al. 2018; You et al. 2020a), and (iii) generally increasing uncertainties and bias in between microwave sensor overpass (e.g., Tan et al. 2016) leading to a misrepresentation of the precipitation features (e.g., size, shape, and orientation) affecting the location and timing of the peak rainfall rates (Guilloteau et al. 2021).

Currently, very few studies have quantitatively tested the ability of these products to retrieve and map extreme rainfall leading to widespread landsliding. In Italy, several SMPPs have been tested to derive rainfall thresholds for landslide and debris flow triggering (Nikolopoulos et al. 2017; Rossi et al. 2017; Brunetti et al. 2018). Overall SMPPs could resolve thresholds, but they were often significantly lower than thresholds estimated from in situ gauging stations and with less discrimination power. Similarly, combining SMPP and soil moisture estimates retrieved from satellite information in California, thresholds for landslide occurrence produced more false alarms than thresholds derived from ground observations (Thomas et al. 2019). Very recently, the spatial pattern of landslides triggered by two storm events in Japan (in 2017 and 2018) was compared with the rainfall pattern retrieved by the Integrated Multi-satellitE Retrievals for GPM (IMERG) product, the ERA5 reanalysis, and ground-based radar observations (Ozturk et al. 2021). In contrast to the ground-based radar observations, neither the reanalysis nor the satellite product estimated higher rainfall amount over the landslide areas than in the surrounding (stable) hillslopes.

Beyond these few case studies, a global assessment of SMPP to retrieve the properties of rainfall patterns leading to widespread landsliding is still missing. Through the use of ground radar, it was recently shown that the rainfall anomaly (i.e., the ratio between event rainfall and past extreme events) better predicts the spatial distribution of landslides caused by a typhoon in Japan than the absolute amount of rainfall (Marc et al. 2019). The superior ability of rainfall anomaly as an indicator of landsliding may arise from the coevolution of the landscape hydromechanical properties with the extreme climatology (Marc et al. 2019). Additionally, using rainfall anomaly may help to remove systematic errors in mean rainfall retrieval from the SMPPs. Assuming that rainfall anomaly is a valid predictor of landsliding globally, for SMPP to be relevant for landslide hazard alerts, they must retrieve a substantial rainfall anomaly that is spatially collocated with the zone of rainfall-induced landsliding. As the occurrence of widespread landsliding is relatively infrequent, large anomalies retrieved by the SMPPs should also be rare to avoid false alarms.

Here, we focused on 20 storm events for which widespread landsliding has been mapped, to test these two abilities for two high-spatial-resolution (0.1°), long-standing SMPPs [IMERG and Global Satellite Mapping of Precipitation (GSMaP)] and one hybrid product combining model reanalysis and SMPPs [Multi-Source Weighted-Ensemble Precipitation (MSWEP)].

2. Data and methods

a. *Landslide event inventories*

To assess the capability of SMPPs globally, we have tried to gather a large number of landslide inventories spanning a broad range of lithological and climatic settings (Table 1;

TABLE 1. Data summary for the studied rainfall-induced landslide event. Here, I = IMERG, G = GSMaP, M = MSWEP, R = ground-based radar, L = Lightning, g = gauges, and NA = not available. Abbreviations for lithological units (see Hartmann and Moosdorf 2012) are BA = basaltic, LF = lava flows, MT = metamorphic, SS = siliciclastic, SM = sedimentary, P = plutonic, V = volcanic, A = equatorial, and C = warm temperate. Abbreviations for climatic regimes (see Kottek et al. 2006; Fig. S1 in the online supplemental material) are f = fully humid, s = summer dry, w = winter dry, m = monsoonal, a = hot summer, b = warm summer. For references, 1 refers to Marc et al. (2018), and 2 refers to Emberson et al. (2022). Duration is simply given as an order of magnitude to differentiate short events from intermediate and long ones (also see Fig. S2 in the online supplemental material for some examples of rainfall event time series).

Event place; code; rainfall period	Boundaries (°N; °E)	Landslide distribution area (km^2)	Meteorological data and approximate duration (<10 h/10–30 h/ 30–90 h/>90 h)	3-h/48-h max rainfall intensity (I; G; M) ($mm\ h^{-1}$)	Global lithological map database (GLiM) lithology (Köppen–Geiger climate)	References
Micronesia; MI2; 2 Jul 2002	7/8; 151/153	250	I/G/M + g (10–30 h)	80/15; 30/15; 90/33	BA/LF (Af)	Harp et al. (2004), 1
Kii Peninsula, Japan; J04; 28–29 Sep 2004	33/35; 134/137	200	I/G/M + R (10–30 h)	50/10; 30/5; 130/14	SM/P/MT (Cfa)	Kondo et al. (2004), Shuin et al. (2012)
Taiwan; TW8; 15–18 Jul 2008	21/26; 120/122	3000	I/G/M + g (10–30 h)	50/11; 40/13; 200/50	SM/MT (Cfa)	1
Brazil; B08; 20–25 Nov 2008	−28/−26; −50/−48	1000	I/G/M + g (>90 h)	10/2; 7/1.5; 100/20	MT (Cfa)	Camargo (2015), 1
Taiwan; TW9; 6–9 Aug 2009	21/26; 120/122	11 000	I/G/M + g (30–90 h)	100/25; 30/22; 150/100	SM/MT (Cfa)	1
Italy; IT9; 1 Oct 2009	37/39; 15/16	20	I/G/M + g (<10 h)	10/1; 10/1; 25/3	MT (Csa)	Ardizzone et al. (2012)
Brazil; B11; 11–13 Jan 2011	−23/−22; −44/−42	1500	I/G/M + g/L (10–30 h)	25/4.5; 25/4.5; 80/18	P/MT (Cfa)	1
Kii Peninsula, Japan; J11; 2–5 Sep 2011	33/35; 134/137	5000	I/G/M + R (30–90 h)	45/9; 30/10; 40/18	SM/P/MT (Cfa)	1
Hiroshima, Japan; J14; 20 Aug 2014	33/35; 132/134	30	I/G/M + R (<10 h)	27/3; 23/2; 50/5	P/V/SS (Cfa)	Wang et al. (2015)
Colombia; C15; 17–18 May 2015	5.5/6; −76.5/−75.5	50	I/G/M (<10 h)	25/3; 7/1; 20/3	MT (Af)	1
Myanmar; M15; 15–30 Jul 2015	21/25; 92/95	8000–10 000	I/G/M (>30 h)	15/4; 15/5; 80/30	SM/SS/MT (Cwa)	Mondini (2017)
Dominica; D15; 27 Aug 2015	15/16; −62/−61	700	I/G/M (10–30 h)	55/7; 40/8; 150/33	V (Aw)	UNOSAT (2016)
Haiti; H16; 1–6 Oct 2016	18/19; −75/−72	400	I/G/M (10–30 h)	10/3.5; 15/5; 130/55	V/SM (Aw)	This study
Colombia; C17; 1 Apr 2017	0.5/2; −77/−76	40	I/G/M (<10 h)	10/2; 8/1.5; 60/10	SM/SS (Af)	García-Delgado et al. (2019)
Fukuoka, Japan; J17; 7 Jul 2017	33/34; 130/132	350	I/G/M + g/R (<10 h)	30/5; 25/5; 30/10	V/PY/MT (Cfa)	Ozturk et al. (2021)
Dominica; D17; 18–22 Sep 2017	15/16; −62/−61	700	I/G/M (10–30 h)	25/5; 30/7; 110/29	V (Aw)	van Westen and Zhang (2018)
Philippines; P17; 20–26 Dec 2017	7/8; 123/125	40	I/G (10–30 h)	25/3; 20/3; NA/NA	V (Af)	2
Hiroshima, Japan; J18; 5–8 Jul 2018	33/35; 132/134	2500	I/G + g/R (30–90 h)	45/8; 20/5.5; NA/NA	P/V/SS (Cfa)	Ozturk et al. (2021)
Philippines; P18; 15–20 Sep 2018	16/17; 120/121	50	I/G (10–30 h)	40/6; 30/9; NA/NA	SM/V (Am)	2
Zimbabwe; Z19; 15–19 Mar 2019	−20/−18; 32/34	1000	I/G (30–90 h)	12/4; 20/4; NA/NA	MT/SS (Cwb)	2

Fig. S1 in the online supplemental material), but other events may have been missed or published after we performed data extraction and analysis (e.g., Coe et al. 2014; Prancevic et al. 2020; Emberson et al. 2022). Most of the rainfall landslide event inventories used in this study (see Table 1) are described in previous compilations by Marc et al. (2018) and by Emberson et al. (2022). In addition, we consider the following landslide events with published inventories: Messina 2009 in Italy (Ardizzone et al. 2012), Hiroshima 2014 in Japan (Wang et al. 2015), and Mocoa 2017 in Colombia (García-Delgado et al. 2019). In all of these cases, the boundary of cloud free imagery extends far beyond the extent of mapped landsliding, suggesting the whole footprint of the landslide event is captured and should reflect a change in rainfall amount [when not limited by availability of steep (>10°–15°) hillslopes (Meunier et al. 2007; Lin et al. 2008; Marc et al. 2019)]. In addition, with standard mapping methods (see Stumpf et al. 2014; Marc et al. 2018), we mapped landslides associated with intense rainfall in Japan 2004 (Kondo et al. 2004), Myanmar 2015 (Mondini 2017), and Haiti 2016 (see the online supplemental material).

An important aspect is that the landslides themselves usually have dimensions of 10–100 m and that their exact locations depend on properties varying at fine spatial scale. Thus, we aim to compare the location and dimension of the area where intense landsliding occurred, spanning from ~50 to >10 000 km^2 (Table 1), and where rainfall anomaly was retrieved by the rainfall product with a 0.1° resolution (~100 km^2). To ensure the detection of potentially spatially mislocated anomalies we always extracted rainfall time series over study areas that are substantially broader than the landslide event area (Table 1).

For Micronesia and Dominica, landsliding was dense across the islands, which represents only a few pixels of the rainfall products, and most surrounding pixels were offshore and therefore do not allow us to constrain false positives (i.e., strong anomalies without landsliding). As a result, the interpretation and discussion of the spatial pattern of the anomaly relative to the landslides is more limited.

b. *SMPPs*

Here, we used three SMPPs available from 2000 to the present and with the following spatiotemporal resolution: (i) NASA's 0.1°/30-min IMERG (Huffman et al. 2019), (ii) JAXA's 0.1°/1-h GSMaP (Kubota et al. 2020), and (iii) the 0.1°/3-h MSWEP (Beck et al. 2017), which we describe briefly below.

The IMERG and GSMaP multisatellite precipitation estimates are based on a combination of the thermal infrared (IR) observations from geostationary satellites and the passive microwave (PMW) observations from all the available satellites from the GPM constellation, either imagers or sounders. Additionally, in situ observations from the Global Telecommunication System (GTS) or other gauged-based precipitation products [e.g., Climate Prediction Center (CPC) and GPCC], are used to readjust (a posteriori calibration approach) the satellite precipitation estimates. Although IMERG and GSMaP ingest similar raw data, they differ in their retrieval algorithm.

The V06B IMERG algorithm considers the PMW rainfall retrievals from the Goddard Profiling Algorithm, version 2017 (GPROF2017; Kummerow et al. 2015; Kidd et al. 2015), and the Precipitation Retrieval and Profiling Scheme, version 2019 (PRPS2019; Kidd et al. 2021a). The PMW rainfall retrievals are then combined and intercalibrated with three prior multisatellite algorithms, the TRMM Multisatellite Precipitation Analysis (TMPA; Huffman et al. 2007, 2010), the CPC Morphing–Kalman filter Lagrangian time interpolation scheme (CMORPH-KF; Joyce et al. 2004, 2011), and the Precipitation Estimation from Remotely Sensed Information using Artificial Neural Networks–Cloud Classification System recalibration scheme (PERSIANN-CCS; Hong et al. 2004). Moreover, V06B, incorporates several other major improvements to the algorithm, including, for instance, a homogenous GPM-TRMM calibration, a new model-based morphing scheme and refinements of the Kalman filtering and the quality index. IMERG precipitation estimates are available as two near-real-time outputs (the early and late runs), for which the calibration consists of climatological gauge adjustments (using GPCP), and a post-real-time output (final run–multisatellite precipitation estimate with gauge calibration) that considers monthly gauge analyses for the adjustments.

The V6 GSMaP algorithm utilizes distinct approaches for retrieving the precipitation over land and ocean surfaces, and when orographic rainfall is expected. The retrieval is performed differently depending on the radiometer type through the successive application of three algorithms: the Microwave Imager/Sounder Algorithm (GSMaP_MWIS; Kubota et al. 2007; Aonashi et al. 2009), for calculating the rainfall rate from PMW platforms; the MW-IR Merged Algorithm (GSMaP_MVK; Ushio et al. 2009) using the morphing Kalman filtering approach to better constrain the affected areas and their rainfall rate; and the Gauge-calibrated rainfall algorithm (GSMaP_Gauge; Mega et al. 2019), by adjusting the GSMaP_MVK estimates with the NOAA's global gauge analysis (CPC Unified Gauge-Based Analysis of Global Daily Precipitation). The GSMaP rainfall estimates are available at three levels, namely, real-time, near-real-time, and standard products (GSMaP_MVK and GSMaP_Gauge).

In contrast to IMERG and GSMaP, the MSWEP V2 precipitation estimates are the result of a combination between the gridded precipitation data from satellite estimates, climate model reanalyzes and various global gauge networks (see the list of products in Beck et al. 2017). The methodology underlying MSWEP involves multiple and sequential approaches to take advantage of each of those distinct products to compute the optimal merging of precipitation estimates. In general, it considers distribution and systematic bias corrections, globally and regionally by utilizing daily precipitation observations. Note that MSWEP is not in strict terms an SMPP because it blends satellite measurements with model reanalyzes and rain gauge measurements. Thus, its inclusion aims to assess the pros and cons of GSMaP and IMERG, which have the potential to produce nowcast and hazard alerts for heavy rainfall

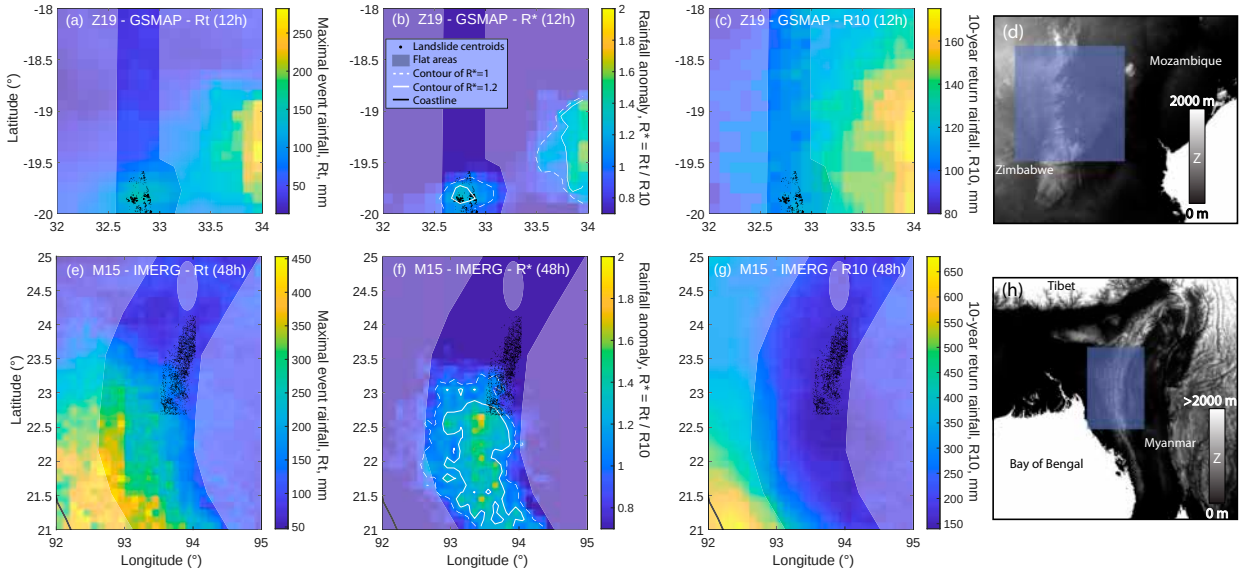

FIG. 1. (left) Maximal total rainfall (Rt; mm), (left center) rainfall anomaly (R^* = Rt/R10), and (right center) 10-yr return rainfall (R10; mm) obtained (a)–(c) from GSMaP at 12-h time scale during Z19 and (e)–(g) from IMERG at the 48-h time scale during M15. Also shown for context are (d),(h) elevation maps of the respective regions containing the study area (in blue). Black dots are landslide centroids, shaded areas are relatively flat terrain where landsliding is unlikely, and white solid and dashed lines in (b) and (e) are the anomaly contour for R^* = 1.2 and 1, respectively. Note that the sharp, linear boundaries of the landslide inventory in (e)–(g) are defined by the footprint of the two Sentinel-2 images that were used for the mapping and that there is evidence of some landsliding occurring beyond these boundaries (see the online supplemental material). Note how the difference in patterns between Rt and R^* is related to the existence of strong spatial gradients in R10.

and landsliding in the coming years (Otsuka et al. 2016; Kotsuki et al. 2019).

Therefore, in our investigation, we have extracted rainfall estimate time series from IMERG Final Calibrated V06B, GSMaP Gauge V6, and MSWEP V2, in regions surrounding each considered landslide event (Table 1). This covers the period from mid-2000 to the end of 2019 for GSMaP and IMERG, but for MSWEP we could only access data until November 2017, which prevented us from studying the four most recent events with this product (Table 1). Given the variable start date of each product, we also discarded the record of each product before 1 January 2001.

c. *Estimation of rainfall anomaly from SMPP*

To assess the relevance of the satellite rainfall products to understand landslide events we propose to use the rainfall anomaly metrics of Marc et al. (2019). The authors found that the spatial distribution of landslides caused by a large typhoon mismatched with the spatial pattern of total rainfall during the typhoon Rt but agreed with the one of rainfall anomaly R^*, defined as

$$R^* = \mathrm{Rt}/\mathrm{R10}, \tag{1}$$

with R10 being the 10-yr return rainfall. The anomaly is defined at each grid cell and over any time scale relevant to landsliding; for example, 3, 12, 48, and 96 h for which both Rt and R10 are computed in this study (Fig. 1). Because it is based on a ratio, the anomaly metric may also remove potential bias of underestimation or overestimation of rainfall in some areas, as long as within a single pixel this bias is systematic through time and thus affects both Rt and R10. Still, some bias is likely to remain as the accuracy of SMPPs' retrieval (especially in rugged terrain or during heavy storms) varies through time, both over yearly and decadal time scales because the satellite constellation has changed, and at the event scale, depending on satellite radar overpasses.

To compute the rainfall anomaly, we first computed R10 for all study areas using the metastatistical extreme value distribution (MEV; Zorzetto et al. 2016). We calculated a time series of mean rainfall rates at a given time scale, excluding every time step where the mean rain rate was below 0.02 mm h^{-1} [~0.5 mm day^{-1}, which is typically in the range of thresholds used to consider dry days (0.1–1 mm day^{-1}; Reiser and Kutiel 2009)] and applied the probability weighted moment method to fit a Weibull (a stretched exponential) distribution to the remaining data of each annual block. Then we derived the MEV cumulative distribution function, as an average of the sample constituted by all the annual Weibull distributions, from which we extracted the 10-yr return rainfall. This method using the whole rainfall dataset is expected to be more robust than fitting a general extreme value (GEV) distribution on the annual maxima (Zorzetto et al. 2016; Marra et al. 2018, 2020). For reference, we have also computed R10 through a maximum likelihood fit of a GEV distribution to the empirical distribution of annual maxima (Saito and Matsuyama 2012, 2015; Marc et al. 2019). This approach yielded R10 maps with similar spatial pattern but with increased magnitude over

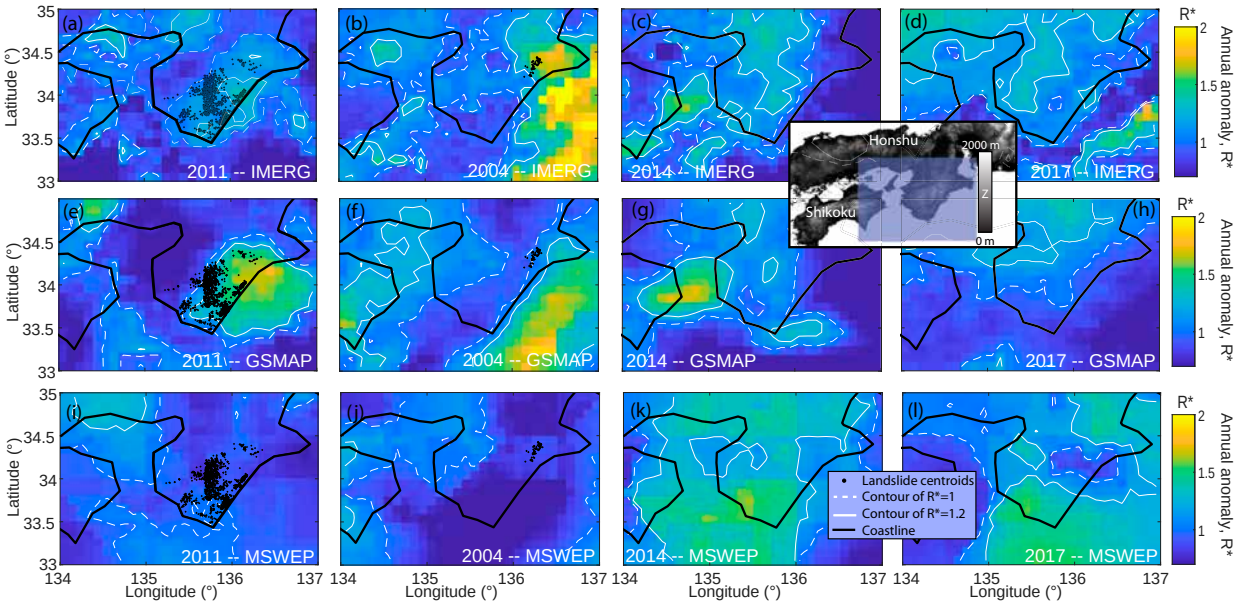

FIG. 2. Maps of the maximal annual anomalies at 48 h, for four selected years over the Kii Peninsula (Japan), for (a)–(d) IMERG, (e)–(h) GSMaP, and (i)–(l) MSWEP. Black dots show landslide centroids from two major landslide events that occurred during Typhoons Meari in 2004 [in (b), (f), and (j)] and and Talas in 2011 [in (a), (e), and (i)]. The timing of these maxima is in Fig. S14 in the online supplemental material. For context, an elevation map of the region containing the study area (in blue) is shown in the inset. Note the difference between products in terms of anomaly retrieval during landslide events in 2011 and 2004, as well as the retrieval large anomalies in 2014 and 2017, although no landslide events were reported.

some zones, typically by 20–100%. Thus, this approach would somewhat decrease the reported anomalies but not change their locations nor our conclusions.

Having mapped R10 over the areas of interest, we compute the maximum total rainfall that occurred over the considered time scales (3–96 h) within a period of 5–15 days containing the storm-induced landsliding event (see Table 1; Fig. 1), as well as within each annual block of the time series. Thus, we estimate the rainfall anomaly both during the event, and for every year of record. This allows us to assess whether a given product did or did not retrieve a strong anomaly associated with large landslide events. It also importantly allows us to assess whether they have recorded rainfall event larger than R10 in the study area (i.e., anomalies with $R^* > 1$) during other time periods (Fig. 2). Note that, if the maximum rainfall rate of the annual block in which the event occurred is outside of the event time window, then the event and annual anomaly will be different.

The four time scales over which both the event and annual anomalies were computed should allow us to capture both landslide events driven by short intense bursts of rainfall and by more prolonged rainfall (see Table 1, along with Fig. S2 in the online supplemental material). We did not use time scales shorter than 3 h because it would exclude the MSWEP product and because the reliability of such short-term measurement on small areas is debated (Guilloteau et al. 2016).

d. Categorizing the accuracy of SMPPs for each event

For each landslide event, we aim to categorize the spatial and temporal accuracy of indicators derived from the SMPPs. Given that the link between landslides and rainfall is not straightforward, fully parameterized extraction and comparison of "rainfall objects" (see Davis et al. 2006) defined based on R^* and landslide density may artificially degrade this link or require too many parameters to be adjusted. These challenges would remain with approaches based on spatial averaging (see Roberts and Lean 2008). However, our objective is not (yet) to develop a specific method to routinely compare landslides and retrieved rainfall, but only to understand in which settings SMPPs retrieve spatial rainfall patterns consistent with the associated landsliding, if at all. By focusing on a few specific cases, one could follow the approach of Ozturk et al. (2021), comparing an empirical model based on static layer only (e.g., slope or geology) with one based on the same static layers complemented with a rainfall map. However, given the number of studied events (20), the number of rainfall anomaly time scales (4) and the number or years evaluated (>15), such an approach would have been impractical and excessive given our goals. Thus, as a preliminary approach for our dataset, we manually inspected each event and evaluated the qualitative agreement of the retrieved anomaly and landslide pattern, through space and time.

To assess the spatial accuracy of the rainfall product qualitatively, we focus on the overlap between significant rainfall anomalies (i.e., $R^* > 1$) and the area of intense landsliding (i.e., ignoring isolated landslides) (Fig. 1). When the overlapping area is similar or larger than the mutually exclusive areas (excluding flat and submerged area with $R^* > 1$), the spatial accuracy is deemed good (Figs. 1b, 2e, and 5d–f and Fig. S7 in the online supplemental material). If the rainfall anomaly

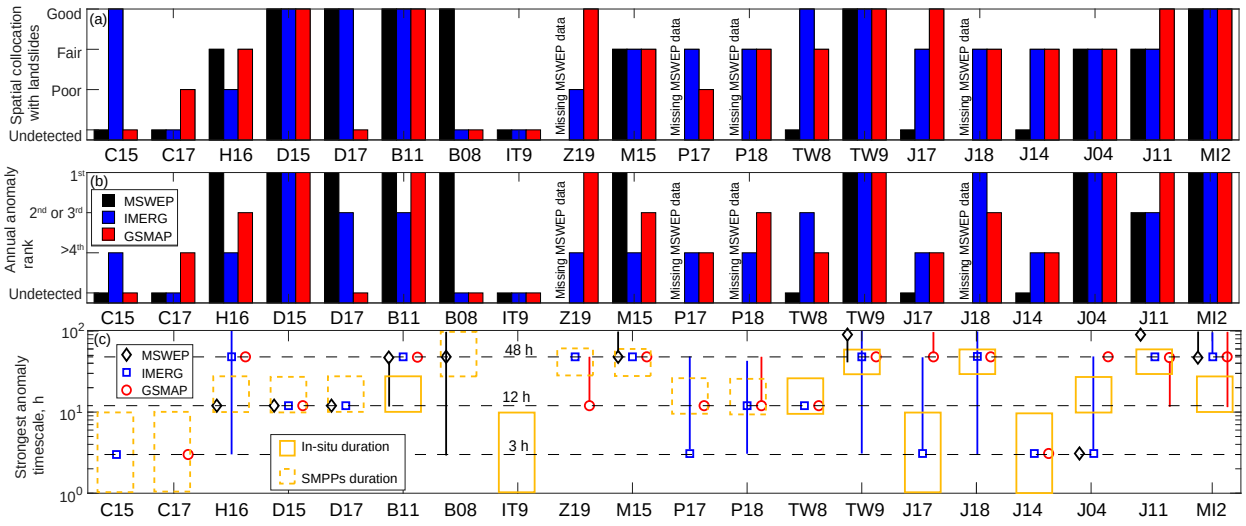

FIG. 3. (a) Spatial and (b) temporal accuracies of the three rainfall products for the 20 rainfall-induced landslide events, labeled by their event code as defined in Table 1. (c) Time scales at which the strongest anomaly occurred for the 20 landslide events and the three rainfall products. In this study we focus on 3, 12, and 48 h, shown by horizontal dashed lines in (c). Vertical bars indicate that similar spatial and temporal performance were obtained at several time scales.

contains the landslide area but extends much beyond, it is ranked as fair (Figs. 2a,b,f). If the rainfall anomaly is offset from the landsliding area but within a range smaller or similar to the dimensions of the landslide event (taken as the small axis of an ellipse containing most of the landslide) it is also deemed fair (Fig. 1e). Finally, when the rainfall anomaly is farther away but still in the study area, it is considered poor (Figs. 2i,j).

The temporal accuracy is based on the intensity of the anomaly within the boundary of the landslide event during the event relative to other annual maxima, since in most areas we have no other substantial landslide events reported over the period (Fig. 2). If the rainfall anomaly was the largest during the last 20 years, the temporal accuracy is the best possible, and false alarms are unlikely. If the rainfall anomaly was ranked second or third, accuracy is fair and false alarms should be rare, while if the anomaly has a lower rank the accuracy is poor and false alarms are likely (Fig. 3). Note that for J04, D17, and TW8, given the affected areas overlap with the larger storms and landslide events that occurred in 2011, 2015, and 2009, respectively (see Table 1 for details and codes for each event), the temporal accuracy is best when the anomaly is ranked second behind these events. In the discussion, we will also address the possibility that another large anomaly retrieved by the SMPP could correspond to other landslide events reported in the literature (especially in Taiwan and Japan) or to landslide events unreported.

When the anomaly at all time scales remains weak ($R^* < 1$) during the event, it is considered undetected by the rainfall product. Given that landslides can be triggered by either short- or long-duration rainfall, for each event we record the time scales yielding the best spatial and temporal accuracies (Figs. S3–S13 in the online supplemental material) and will focus on these time scales in the following results and discussion.

3. Results

In 16 of 20 cases, at least two products have detected a substantial anomaly ($R^* > 1$) over at least one time scale during the events triggering landsliding (Fig. 3). However, we note that the rainfall products have fairly diverse spatial and temporal accuracies, even though they used the same satellite constellation as a primary source of data. Below, we briefly detail this diversity of performance by reviewing each case. Note that except for MSWEP for J11, the 96-h time scale never performs better than shorter time scales (Fig. 3c), and thus will not be described in detail.

a. Case-by-case anomaly patterns and accuracy

For some events, all products retrieved similar anomaly patterns, such as MI2, and D15 where all products retrieved $R^* > 1.5$–2 all over the impacted island (Micronesia or Dominica) at 48 and 12 h, respectively. Similarly, for B11 at 12–48 h and TW9 at 48 h, all products retrieved an anomaly in or near the landsliding area of $R^* \sim 1.4$ and $R^* \sim 1.5$–2, respectively. For these four cases the event anomalies were the largest in the area for 20 years. For M15, all products also retrieved $R^* \sim 1.2$–1.4 at 48 h, on the southern edge of the landslide area (Fig. 1) but the temporal accuracy varied, as the event anomaly was ranked first, third, and beyond sixth for MSWEP, GSMaP, and IMERG, respectively. For J04, all products retrieved an anomaly ($R^* \sim 1$–1.5) over the landslide area and ranked it as the largest in the northeastern part of the Kii Peninsula for the last 20 years. However, MSWEP and IMERG had the anomaly spreading over a much larger area than the one experiencing landsliding, and the time scales with the strongest anomaly varied from 3 to 48 h for the three products (Fig. 3). For P18, both GSMaP and IMERG retrieved $R^* \sim 1.2$ at 12 h on the eastern edge of the landslide zone, but none retrieved

this anomaly as the strongest of the time series. Similarly, for J18, both GSMaP and IMERG retrieved $R^* \sim 1.2$–1.4 at 48 and 12 h, respectively, on the eastern edge of the landslide zone but found a stronger anomaly to have occurred in October 2017.

Other landslide events are not retrieved in terms of rainfall anomalies. For H16, MSWEP retrieved $R^* > 1.4$ over the whole peninsula at 12–48 h, GSMaP found $R^* \sim 1$–1.2 at 48 h, localized at the peninsula's tip, and IMERG found a localized anomaly of $R^* \sim 0.9$–1 for 10–20 km east of the landslide event area. For J11 at 48 h, GSMaP and IMERG found $R^* \sim 1$ and $R^* > 1$–1.4 in the landslide event area and ranked first and third annual anomaly of the time series, respectively. MSWEP yield similar results but only at 96 h. J14 was not detected by MSWEP, but both GSMaP and IMERG found an anomaly ($R^* \sim 1$) at the 3 h time scales, next to the landslide area but with many false alarms (larger anomalies) recorded for other years. We note that the anomaly is a bit stronger at 2 h, which makes sense given the intense rainfall was just limited to 2 h (Wang et al. 2015). For J17, MSWEP did not detect any anomaly, and GSMaP and IMERG detected a localized $R^* \sim 1$–1.2 overlapping with or 10 km eastward, respectively, of the landslide event. For TW8, MSWEP did not retrieve a significant anomaly, while IMERG found $R^* \sim 1$–1.2 at 12 h mostly collocating with the landslide clusters, and GSMaP found an anomaly of $R^* \sim 1.2$ located mostly on the flat coast west of the landsliding. For P17, MSWEP was not available and both SMPPs retrieved some pixels with $R^* \sim 1$–1.2 near the landslide events, but they all had many other years with similar annual anomalies. For Z19, both SMPPs found $R^* > 1.5$ at 12–48 h more than 100 km east of the landslide event, over flat areas, and only GSMaP found $R^* \sim 1.4$ precisely collocated, in space and time, with the landslide event.

Last, some events were retrieved by only one product, such as B08 where MSWEP only found a localized $R^* > 1$ at all time scales, C15 where only IMERG detected $R^* > 1$ locally, and C17 where only GSMaP found $R^* \sim 1$–1.2 but about 100 km northeast of the landslide event. IT9 was undetected by the three products.

b. *Global performance and relation to time scales*

For the studied events, the three products have similar performance spatially and temporally, with only a third of good retrieval, and with some false alarms and poor to fair localization in most cases. For each product, the spatial and temporal accuracies are quite strongly correlated, although IMERG often has the best spatial accuracy, while GSMaP often has the best temporal accuracy (Fig. 3, along with Fig. S15 in the online supplemental material). Given our limited landslide inventory sample, we do not attempt to evaluate how the capability of different products varies in different geographical regions. However, we note that the capability of the products does not seem related to the year of the event, with some poorly retrieved events occurring both in the TRMM era (B08, IT9, and TW8) and the GPM era (C15, C17, and P17).

Despite the variable ability to retrieve a spatial anomaly collocated with landsliding or to rank the annual events from 2001 to 2019, the three products agree most of the time in terms of the time scale over which the maximal rainfall anomaly occurred during the landslide event (Fig. 3c). Indeed, in most of the Asian and Pacific Ocean typhoon cases (TW9, J11, J18, and M15), the products display the strongest anomaly with the best spatial match at the 48-h hour time scale. This appears to be the good order of magnitude for the intense rainfall duration between 1 and 3 days (Table 1). For TW8, D15, D17, and P18 all products suggest the anomaly best related to the landsliding was at the 12-h time scale, which can only be confirmed from in situ data for TW8. Although more uncertain and retrieved only by some products, C15, C17, and J14 only have anomalies at 3-h time scales consistent with the ideas that they were short, localized intense rainfall (Wang et al. 2015).

For six other cases (MI2, H16, P17, J04, J17, and Z19), the time scales of different products disagree and do not necessarily match the duration of absolute rainfall records.

4. Discussion

a. *On the importance of normalizing absolute rainfall estimates*

We note that although the three products often had rainfall anomalies that showed similar patterns in terms of spatial and temporal patterns, they would have been much more difficult to compare with absolute values. Indeed, in terms of absolute rainfall the location and amount retrieved by the three SMPPs could easily vary by more than a factor of 2, making any quantitative comparisons between the products and empirical or physical thresholds very difficult.

For example, during Typhoon Morakot (TW9) and Meari (J04), the total rainfall during 48 h over the area with widespread landsliding was about 800 and 500 mm for IMERG, 1200 and 250 mm for GSMaP and 4000 and 700 mm for MSWEP, respectively (Fig. 4, along with Fig. S7 in the online supplemental material). For the area with landsliding in M15 and J11, the 48-h total rainfall was about 300 and 400 mm, respectively, for both IMERG and GSMaP, while in the same area MSWEP reported about 1500 and 800 mm, respectively. Independent gauge or ground-based radar estimates available for TW9, J04, and J11 suggest that 48-h rainfall amounted to about 2000, 800, and 1000 mm (Kondo et al. 2004; Chien and Kuo 2011; Marc et al. 2019), suggesting that none of the SMPPs were correct and that it would be very difficult to build and compare threshold in terms of absolute rainfall. Similar bias and variability can be found at short time scales, for example, in 3 h during the J14 event in the landsliding area, GSMaP and IMERG recorded about 75 mm in 3 h while MSWEP recorded 150 mm. All products underestimated the event rainfall measured by ground-based radar to 220 mm in 3 h (Wang et al. 2015), but, interestingly, although MSWEP was the closest in absolute terms it is the only product that did not yield any anomaly, since the R10 in this area is 250 mm (Fig. S8 in the online supplemental material). These large differences in absolute rainfall at short and long time scales likely come from the fact that different gauges are used for normalization and that GSMaP uses an orographic rainfall boost under some conditions, while MSWEP

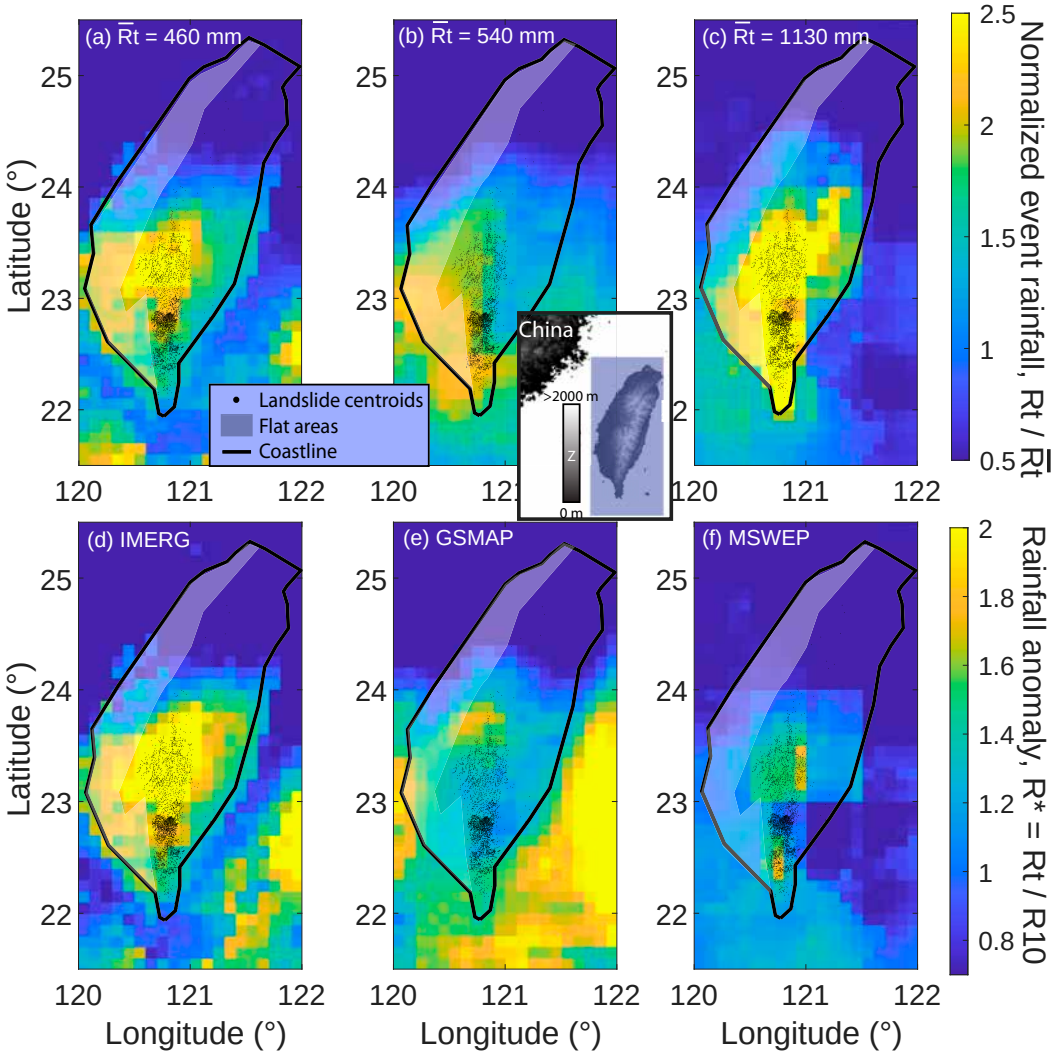

FIG. 4. Maps of (a)–(c) total event rainfall normalized by the mean event rainfall over the study area and (d)–(f) rainfall anomaly at 48 h during Typhoon Morakot for the three rainfall products, as labeled. For context, an elevation map of the region containing the study area (in blue) is shown in the inset. Centroids of landslides triggered by Morakot are in black, and flat coastal areas not prone to landsliding are within the shaded area. Note the diversity of patterns and magnitude of absolute rainfall among rainfall products and how it is reduced when computing rainfall anomaly.

may, in some cases, revert to the reanalysis modeled rainfall rather than the satellite measurements. For the 20 storm events, the diversity of mean rain rates leading to landsliding (whether at short or long time scales) is also very large from about 5 to >100 mm h^{-1} (Table 1), which underlines the difficulty in looking for global threshold in absolute rainfall intensity.

Beyond intercomparison with thresholds, the effect of a normalization by R10 also allows us to account for strong gradients in the local climatology of extremes that could mislead landslide hazard warnings. For example, M15 and Z19 both have much larger Rt values toward the coast, in relatively flat areas, and it is when computing R^* that it becomes clear that the mountainous areas had actually exceptional rainfall with $R^* > 1.2$ on or near the landslide event area (Fig. 1).

b. *Are other extreme anomalies false alerts or unreported landslide events? Insights from Taiwan and Japan*

Among the studied areas, only some parts of Taiwan have been mapped sufficiently frequently to identify landsliding caused by multiple typhoons within the same areas. Marc et al. (2015) mapped the landslides caused by rainfall events between 1996 and 2014 within the Chenyoulan catchment in central Taiwan (23.5°–24°N). Huang and Montgomery (2012) reported intense landslides in 2001, 2004 and 2005 along the Tachia River (about 24°N), while Chen et al. (2013) mapped the impact of more than 10 typhoons in three catchments across Taiwan (Fig. 5). Given that not all of these studies report landslide area density, as a first-order test we use landslide number density as a measure of the relative magnitude of the landslide event caused by

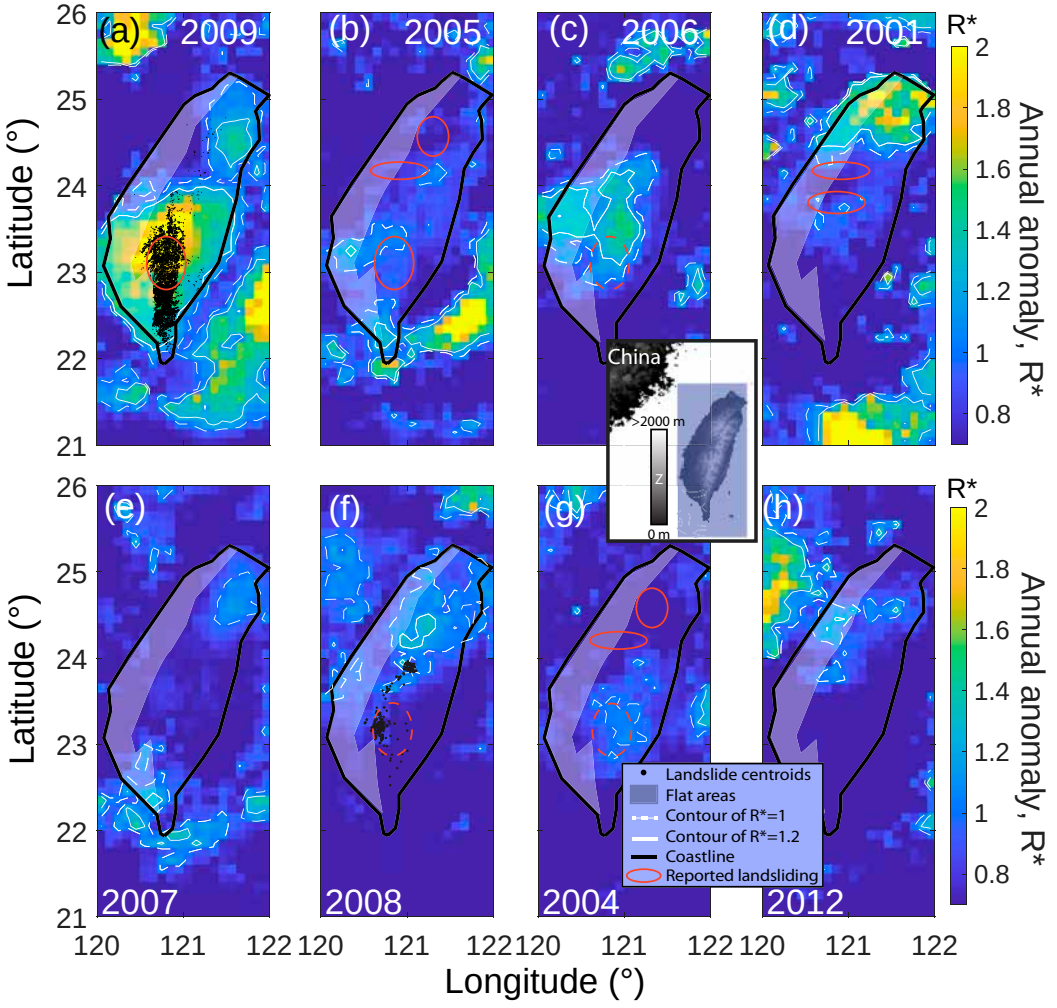

FIG. 5. (a)–(h) The eight strongest maps of annual maxima of 48-h rainfall anomalies from IMERG over Taiwan. For context, an elevation map of the region containing the study area (in blue) is shown in the inset. Landslides centroids from TW8 and TW9 are shown as black dots in (a) and (f). Major landslide events reported from the literature (see text) are outlined in solid red (intense landsliding: >0.5 km^{-2}) or dashed red (moderate landsliding: 0.1–0.5 km^{-2}). Results are similar for MSWEP and GSMaP. The timing of these maxima is in Fig. S16 in the online supplemental material. Note that, although we have accessed only two comprehensive landslide inventories [shown in (a) and (f)] many years with $R^* > 1$ actually also had reported landsliding during the typhoons that caused these anomalies [(b)–(d) and (g)].

various typhoons. In the northern catchment (24.5°N), they could constrain only the typhoons between 2004 and 2009 and found that intense landsliding (>1 per km^2) occurred in August 2004 and 2005, during Typhoons Aere and Matsa, respectively. In the two southern catchments (23°N) they reported most landslides during Morakot (TW9, >1 km^2), and second most during Typhoon Haitang in July 2005 (~0.5 km^2). Three other typhoons induced similar landsliding (0.1–0.2 km^2); Typhoons Mindulle, Bilis, and Kalmaegi (here TW8), in early July 2004, 2006, and 2008, respectively, while other events caused significantly fewer landslides.

In Taiwan, the pattern and timing of the maximum annual anomalies is quite similar for the three SMPPs, and the following discussion applies to all SMPPs. In September 2001, a very strong anomaly hit northern Taiwan (25°N) corresponding to Typhoon Nari, while a more modest anomaly in late July near 24°N corresponding to Typhoon Toraji, which caused widespread landsliding between 23.5° and 24°N (Huang and Montgomery 2012; Marc et al. 2015). Substantial anomalies are also present from 24° to 22°N in July 2005 and near 24°N in July 2006, matching well with Typhoons Haitang and Bilis, although the anomalies are not as large in 2005 as might be expected from the landsliding and the gauge measurements (Chen et al. 2013, 2015). Surprisingly, the typhoons that caused landsliding in the north in 2004 and 2005 (Aere and Matsa) have not been recorded with strong anomalies

(Figs. 5b,g). However, from 24.5° to 25.5° moderate but extensive anomalies were retrieved in October 2007 and September 2008, matching with Typhoons Krosa and Sinlaku, which caused some landslides in northern Taiwan (Chen et al. 2013). However, these two years the typhoons causing landslides in the south (Sepat in 2007 and Kalmaegi in 2008) were not retrieved consistently with the poor spatial and temporal score achieved for TW8 (Fig. 3). These results strongly suggest in the case of Taiwan that across the last decades many of the largest anomalies were indeed significant typhoon events that caused landsliding (Fig. 5), and the poor score of TW8 seems to be more likely due to some misdetection of this event rather than false alarms for other typhoons. Nevertheless, the rainfall anomaly in 2001 (Nari) and 2012 appears as a false alarm, and several rainfall-induced landslide events are associated with $R^* < 1$ or mislocated anomalies (Fig. 5).

Japan is also very prone to landslides, frequently leading to media or scientific reports. Below, we discuss major anomalies and landslide reports from the literature in the three areas we have analyzed.

In the Kii Peninsula, the interproduct variability is higher than in Taiwan but we note that GSMaP, and to some extent MSWEP, retrieve substantial anomalies ($R^* \sim 1$–2) on the southern and eastern part of Shikoku island (134°E) in August 2004 (Fig. 2). This corresponds to the heavy rainfall caused by Typhoon Namtheum, which led to several large landslides in Shikoku island (Wang et al. 2005). In contrast, all SMPPs detect significant anomalies ($R^* > 1.5$) on the eastern edge of Shikoku in 2014 and across the peninsula in 2017, while we did not find any reports of landslides for those two years.

Over Kyushu, both SMPPs yield several annual anomalies equal or larger to that observed in 2017, but we could not find mention of other landslide disasters in the area in the literature or the international disaster Emergency Events Database (EM-DAT). Over Hiroshima, J18 is clearly among the largest anomalies, but October 2017 also appears as the first and second largest anomaly for GSMaP and IMERG, respectively. It corresponds to Typhoon Lan, which caused flooding and some landsliding over several prefectures of Honshu island (EM-DAT). Additionally, even if J14 yields $R^* \sim 1$ at short time scales, well collocated with landsliding, many years have stronger anomalies without reported landsliding, suggesting some underestimation.

In summary, in Taiwan, most annual maxima of rainfall anomaly correspond to major typhoons that have caused landslides and the major challenge for the products is rather that some events are underestimated. In Japan, it is less clear, and while some major anomalies correspond to other landslide or flooding events (Shikoku 2004; Hiroshima 2017), we also find that several annual anomalies may be overestimated. Such false alerts and overestimation of the anomaly may be due to an underestimation of R10 in some places rather than to the overestimation of the event rainfall. We also note the likelihood of false alarms derived from anomaly ranking is a very rough measure, which has multiple limitations. First, this technique was not evaluated globally on all landslide prone terrain, but also because we focus on a threshold of $R^* > 1$ while this threshold likely varies, for example with lithological units (Marc et al. 2019). This highlights the need for future studies to better understand the source of uncertainties of $R10$ for each product, as well as to replicate the methods in other geographical areas and with other, landscape adjusted, R^* threshold.

c. *Limits and potential for improvement of the SMPPs*

We have assessed the relevance of SMPPs to landslide analyses with the working assumption that landslide events are bound to occur on any hillslopes experiencing rainfall amounts (over time scales from 3 to 96 h) exceeding the local 10-yr return rainfall, as shown for J11 (Marc et al. 2019). This approach is consistent with the geomorphological concept (Dietrich et al. 1995; Iida 2004; Marc et al. 2019) that the stability of the landscape is adjusted to the climate and in particular the extreme meteorology.

We note that performing the same analysis over 192 h (8 days) did not improve the results, which may not be surprising given that all events except B08 are shorter than 100 h. However, the focus on rainfall anomalies ignores the fact that landslides are caused by a rise of pore water pressures that may only partially relate to the ongoing rainfall, and in large part are due to antecedent rainfall and hydrological processes modulating the subsurface drainage (Bogaard and Greco 2018) and the water storage in the slope aquifer (Brönnimann et al. 2013; Watakabe and Matsushi 2019), with all these processes being modulated by the slope fabrics and fracturing. As a result, a future approach could aim to couple a simple model to estimate the water level in the regolith based on the rainfall time series (e.g., Wilson and Wieczorek 1995) and focus on anomalies of regolith water level (e.g., Saito and Matsuyama 2012). Combining rainfall products with satellite-based soil moisture estimates could also be a way forward (Felsberg et al. 2021). Still, in the cases of sustained heavy rainfall caused by typhoons and hurricanes, overrepresented in this study, the moisture from antecedent rainfall is likely negligible relative to the one brought by the event. Beyond antecedent rainfall, the rainfall regime as well as hydromechanical properties of the ground modulate landslide triggering, likely affecting the ability of SMPPs to retrieve the conditions of landsliding. Although our global analysis covers many typical landslide settings (Table 1), it does not sample them equally, especially in terms of climate (temperate and equatorial fully humid settings represent more than half our database). Additionally, some specific settings are not represented such as landscapes with carbonates topography, or with "arid," "snow," or "polar" climates; these are less common but present in areas prone to landsliding such as the Alps, Norway, central Asia, and the edges of the Tibetan Plateau (Fig. S1 in the online supplemental material). Future studies should aim to constrain these undersampled settings, and to evaluate SMPPs in specific settings that may be associated with peculiar landslide triggering (e.g., orography, atmospheric rivers, rain-on-snow events, monsoons, and very long-duration–weak-precipitation events).

1) SELECTED EVIDENCE OF INCORRECT RAINFALL RETRIEVAL

For a number of rainfall-induced landslide events, we lack independent rainfall in situ measurements. Thus, the discrepancy between satellite anomaly maps and landslide locations

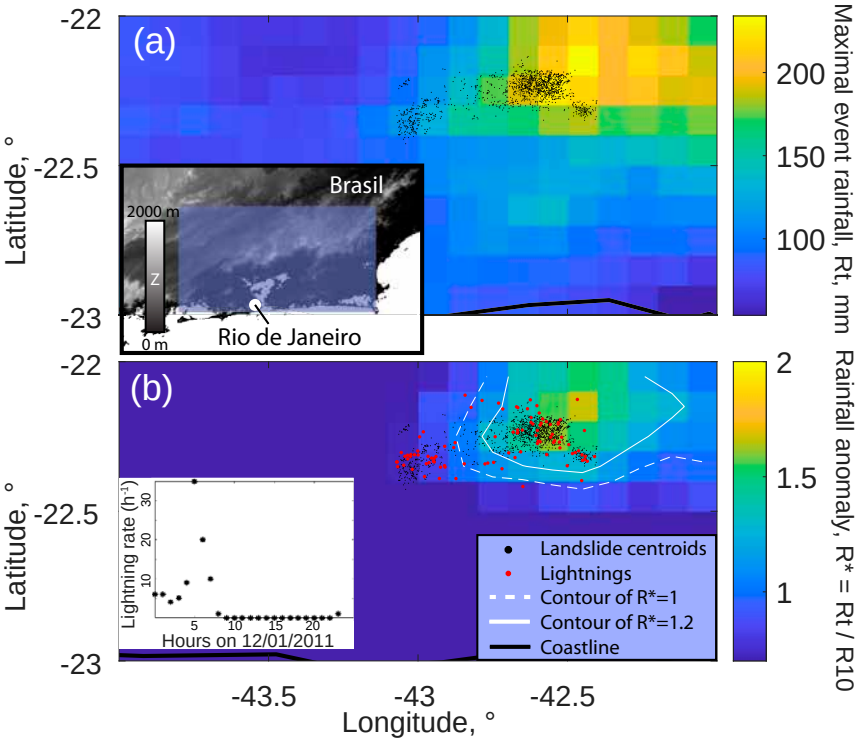

FIG. 6. (a) Maximal event rainfall and (b) anomaly at 48-h time scale for GSMaP during B11. For context, an elevation map of the region containing the study area (in blue) is shown in the inset. Black dots are landslide centroids, and white solid and dashed lines in (b) are anomaly contour for $R^* = 1.2$ and 1, respectively. Results are almost identical for IMERG and MSWEP. Recorded lightning locations on 12 Jan are shown by red dots in (b), and their timing is in the inset. In comparison, lightning activity on 11 and 13 Jan was much weaker. Note that the cluster of landslides near −22.3°N, −43°E is outside the contour of $R^* > 1$ but is well correlated with lightning activity, which likely relates to intense localized convection and rainfall.

may not necessarily be due to a misretrieval of the rainfall by the SMPP but could also be due to some additional variability in factors controlling the landslide location, such as the strength, permeability and infiltration rate, slope gradient, and vegetation state of hillslopes. However, in several cases, in situ rainfall data reported intense rainfall activity collocated with the landsliding, which suggests that the SMPP rainfall retrieval is in large part at fault. This was clearly the case for J11 where the rainfall anomaly estimated from ground-based radar agreed precisely with the area of landsliding (Marc et al. 2019). The same was true when considering total event rainfall for J17 and J18 (Ozturk et al. 2021). This was also likely the case for TW9 and IT9, which all had exceptional levels of absolute rainfall in the area where most landslides occurred (Chien and Kuo 2011; Ardizzone et al. 2012). On these four events, only TW9 was well retrieved by all products, though even in this case the quantitative pattern of R^* at fine scale is very different in each case (Fig. 4). The retrievals for the Japanese cases (J11, J17, and J18) were variable, and IT9 was completely undetected by the three products.

The two Brazilian landslide events (B08 and B11) also highlight the issue with the current retrieval of SMPPs. B08 was completely undetected by GSMaP and IMERG, and the detection by MSWEP may be entirely due to a local gauge nearby (Camargo 2015) that recorded heavy rainfall on the two days preceding the events, at the end of an anomalously wet month.

For B11, the three SMPPs broadly agreed during the event and retrieved a strong anomaly between 12 and 48 h, overlapping with most of the landsliding slightly offset to the northwest of the landsliding area (Fig. 6). For this event, the Brazilian lightning record shows intense lightning activity precisely collocated with the three clusters of landsliding (Fig. 6). The link with the landslides is even more striking considering that most of the lightning on this day occurred between 0500 and 0700 local time, which matches well with the timing of several destructive landslides in urban areas reported between 0600 and 0900 LT 12 January (Netto et al. 2013).

Strong lightning activity at the time of landsliding was reported for older disasters in Brazil (Jones 1973), even leading to the suggestion that they may directly induce landsliding (Lacerda 1997). However, it is well known that lightning activity is associated with intense convection and intense bursts of rainfall (Battan 1965; Piepgrass et al. 1982; Soula and Chauzy 2001; Schultz et al. 2011), which strongly suggests that exceptional rainfall intensity must have occurred on the

morning of 12 January, exactly when the landslide occurred, from 42.5° to 43°W. In contrast the three SMPPs suggested a lower values of both Rt and R^* from 42.5° to 43°W (Fig. 6).

Thus, we propose that, in many of the studied cases, the poor link between SMPP retrieval and landslide location is likely due to inadequate rainfall retrieval from the SMPP rather than due to some independent complexities in the landscape and/or the landslide mapping. In the next section we briefly identify options to improve the SMPP algorithms.

2) Improving SMPP retrieval for landslide applications: Including lightning and orography

As we have seen in the case of B11, the spatiotemporal pattern of lightning seems to accurately match the location of landsliding. Thus, with the recent launch of the Geostationary Operational Environmental Satellite (GOES) satellite, with sensors permitting mapping of lightning activity [Geostationary Lightning Mapper (GLM)] with high spatiotemporal accuracy (Goodman et al. 2013), incorporating lightning activity in SMPPs is potentially a way forward to improve mapping of extreme rainfall and landslide applications. Physical models to derive quantitative precipitation estimates from lightning activity exist (Minjarez-Sosa and Waissman 2017) and could be used in conjunction with other highly resolved, continuous measurements (such as the geostationary infrared in PERSIANN; Xu et al. 2013; Mahrooghy et al. 2013). This may prove especially useful in capturing brief and localized events that may form and dissipate without being sampled by the passive microwave radiometers, likely strongly biasing their retrieval (Guilloteau et al. 2017). In fact, SMPPs tend to smooth rainfall rate over scales smaller than 200 km and 4 h, biasing both the intensity, location, and timing of precipitation features (Guilloteau et al. 2021). More generally, uncertainties in SMPPs rain retrieval are highly space–time dependent, as it depends both on environmental conditions (e.g., the precipitation regime, type of precipitation system, surface type), and the technique itself, which involves the combination of distinct uncertainty sources (i.e., the calibration, the algorithm, and the sampling terms; Roca et al. 2010). Particularly among these factors PMW observations, which are the essential component of IMERG and GSMaP, are commonly processed through Bayesian-like algorithms (Aonashi et al. 2009; Kummerow et al. 2015), implying certain limitations, for instance in dealing with the platform-sensor heterogeneity and the rainfall rate variability. Consequently, both the intensity and detection of light and intense rainfall may be biased (Elsaesser and Kummerow 2015; Kidd et al. 2018; You et al. 2020b), which also propagates up to the final level-3 precipitation retrieval (Ayat et al. 2021; Oliveira et al. 2016).

Another issue that may bias SMPPs, especially in the case of landslide studies, is the retrieval of orographically forced rainfall. Studies focused on Japan, Taiwan, and India, have shown that the satellite radar profile with altitude was strongly affected in the case of upward orographic forcing of warm and humid air masses (Shige et al. 2013; Taniguchi et al. 2013; Yamamoto et al. 2017). As a result, the GSMaP algorithm was updated to differentiate for such orographic conditions, based on reanalyzed wind model and topography. However, the issues in overestimating or underestimating the orographic effect depending on the wind speed has been highlighted for GSMaP v6 and should be corrected in v7 (Yamamoto et al. 2017). Unfortunately, GSMaP v7 has not been reprocessed before 2014 yet and our results are based on v6 and therefore suffer from this inaccurate orographic algorithm. This issue also strongly impacts the maps of R10 (Figs. S7c and S10c in the online supplemental material), leading in the case of TW9 and TW8 to a strong reduction of the anomaly relative to the other SMPPs (Fig. 4, along with supplemental Fig. S10). In the case of J11 this issue is less pronounced and despite it GSMaP retrieves a much stronger anomaly (the strongest on record) although a bit offset from the main relief (Fig. 2). In any case, investigating and updating the orographic algorithm to prevent this bias in rainfall location seems urgent to maximize GSMaP relevance for landslide studies. Further developing orographic corrections, to also account for other forms of orography other than the uplift of warm and humid air masses is also of importance (see review by Houze 2012).

Last, efforts to improve high-resolution SMPPs are constantly ongoing (see Kidd et al. (2021b) for a detailed review), such as adaptation of the PMW algorithms to better deal with distinct surface environments (Turk et al. 2021), or correctly filling the gaps between the PMW and IR observations (Tan et al. 2021), which are expected to improve the applicability of SMPPs for landslide applications.

5. Conclusions

We have analyzed the rainfall during 20 storm events that caused widespread landsliding, as recorded by three rainfall products based (partially or totally) on satellite measurements. Specifically, we have focused on the recorded rainfall anomaly, that is, the maximal rainfall over a given time scale, normalized by the 10-yr return rainfall over the same time scale. Although the spatiotemporal pattern of retrieved anomalies varies somewhat from product to product, at least one product coincides at least partially with the area of widespread landsliding in 11 cases, and the rainfall event that caused landsliding was retrieved as the largest anomaly of the observation period in 12 cases. Typhoons and hurricanes with rainfall lasting several days over large areas are most often retrieved as substantial anomalies, often at the 48-h time scale, while landslide events caused by short, localized rainfall seem to be the hardest to retrieve. In any case, we found that using anomalies allows us to remove substantial interproduct variability and bias in the absolute estimate of rainfall, and in some cases to better relocate the area with high landslide hazard. Thus, we suggest that implementing the normalization of satellite rainfall using long-term records is necessary in an operational landslide hazard awareness algorithm (e.g., Kirschbaum and Stanley 2018). Still, there is large room for improvement in the satellite product to better constrain the 10-yr rainfall and the rainfall events, possibly by better integrating spatial information from lightning activity and orographic processes, which are often important in mountainous areas. Also, to improve the

operational use of rainfall anomalies, future studies should evaluate how to define anomalies combining early and nowcast products (Otsuka et al. 2016; Kotsuki et al. 2019) with long-term rainfall products to derive extreme climatology, and the impact of the evolution of satellite constellation on the estimation of the 10- or 20-yr return rainfall.

Acknowledgments. The authors declare no conflict of interest. We thank Ben Mirus and two anonymous reviewers for constructive comments that helped to clarify and strengthen the paper. We are grateful to E. Zorzetto for distributing his codes to compute the metastatistical extreme value distribution (https://github.com/EnricoZorzetto/mevpy).

Data availability statement. The disaster database information is available at EM-DAT, CRED/UC (https://www.emdat.be/; D. Guha-Sapir, last accessed 10 December 2021). The GPM IMERG Final Precipitation L3 Half Hourly 0.1° × 0.1° V06B data were obtained from the Goddard Earth Sciences Data and Information Services Center (GES DISC; https://doi.org/10.5067/GPM/IMERG/3B-HH/06). The GSMaP Gauge Precipitation L3 Hourly 0.1° × 0.1° V6 data were acquired online (https://sharaku.eorc.jaxa.jp/GSMaP/). The MSWEP 3-hourly 0.25° global gridded precipitation V2 data were freely accessed online (http://www.gloh2o.org). The landslide database is accessible through the different works listed in the references.

REFERENCES

AghaKouchak, A., A. Behrangi, S. Sorooshian, K. Hsu, and E. Amitai, 2011: Evaluation of satellite-retrieved extreme precipitation rates across the central United States. *J. Geophys. Res.*, **116**, D02115, https://doi.org/10.1029/2010JD014741.

Amatya, P., D. Kirschbaum, T. Stanley, and H. Tanyas, 2021: Landslide mapping using object-based image analysis and open source tools. *Eng. Geol.*, **282**, 106000, https://doi.org/10.1016/j.enggeo.2021.106000.

Aonashi, K., and Coauthors, 2009: GSMaP passive microwave precipitation retrieval algorithm: Algorithm description and validation. *J. Meteor. Soc. Japan*, **87A**, 119–136, https://doi.org/10.2151/jmsj.87A.119.

Ardizzone, F., and Coauthors, 2012: Landslide inventory map for the Briga and the Giampilieri catchments, NE Sicily, Italy. *J. Maps*, **8**, 176–180, https://doi.org/10.1080/17445647.2012.694271.

Ayat, H., J. P. Evans, and A. Behrangi, 2021: How do different sensors impact IMERG precipitation estimates during hurricane days? *Remote Sens. Environ.*, **259**, 112417, https://doi.org/10.1016/j.rse.2021.112417.

Battan, L. J., 1965: Some factors governing precipitation and lightning from convective clouds. *J. Atmos. Sci.*, **22**, 79–84, https://doi.org/10.1175/1520-0469(1965)022<0079:SFGPAL>2.0.CO;2.

Baum, R. L., J. W. Godt, and W. Z. Savage, 2010: Estimating the timing and location of shallow rainfall-induced landslides using a model for transient, unsaturated infiltration. *J. Geophys. Res. Earth Surf.*, **115**, F03013, https://doi.org/10.1029/2009JF001321.

Beck, H. E., and Coauthors, 2017: Global-scale evaluation of 22 precipitation datasets using gauge observations and hydrological modeling. *Hydrol. Earth Syst. Sci.*, **21**, 6201–6217, https://doi.org/10.5194/hess-21-6201-2017.

Bogaard, T., and R. Greco, 2018: Invited perspectives: Hydrological perspectives on precipitation intensity-duration thresholds for landslide initiation: Proposing hydro-meteorological thresholds. *Nat. Hazards Earth Syst. Sci.*, **18**, 31–39, https://doi.org/10.5194/nhess-18-31-2018.

Brönnimann, C., M. Stähli, P. Schneider, L. Seward, and S. M. Springman, 2013: Bedrock exfiltration as a triggering mechanism for shallow landslides. *Water Resour. Res.*, **49**, 5155–5167, https://doi.org/10.1002/wrcr.20386.

Brunetti, M. T., M. Melillo, S. Peruccacci, L. Ciabatta, and L. Brocca, 2018: How far are we from the use of satellite rainfall products in landslide forecasting? *Remote Sens. Environ.*, **210**, 65–75, https://doi.org/10.1016/j.rse.2018.03.016.

Caine, N., 1980: The rainfall intensity: Duration control of shallow landslides and debris flows. *Geograf. Ann.*, **62A**, 23–27.

Camargo, L. P., 2015: Análise integrada no meio físico dos ribeirões Braço Serafim e Máximo com ênfase nas áreas de fragilidade estrutural, Luís Alves, (SC). Ph.D. thesis, Universidade Federal de Santa Catarina, 193 pp., https://repositorio.ufsc.br/handle/123456789/157291.

Chen, Y.-C., K. Chang, Y.-J. Chiu, S.-M. Lau, and H.-Y. Lee, 2013: Quantifying rainfall controls on catchment-scale landslide erosion in Taiwan. *Earth Surf. Processes Landforms*, **38**, 372–382, https://doi.org/10.1002/esp.3284.

——, ——, H. Lee, and S. Chiang, 2015: Average landslide erosion rate at the watershed scale in southern Taiwan estimated from magnitude and frequency of rainfall. *Geomorphology*, **228**, 756–764, https://doi.org/10.1016/j.geomorph.2014.07.022.

Chien, F.-C., and H.-C. Kuo, 2011: On the extreme rainfall of Typhoon Morakot (2009). *J. Geophys. Res.*, **116**, D05104, https://doi.org/10.1029/2010JD015092.

Coe, J. A., J. W. Kean, J. W. Godt, R. L. Baum, E. S. Jones, D. J. Gochis, and G. S. Anderson, 2014: New insights into debris-flow hazards from an extraordinary event in the Colorado Front Range. *GSA Today*, **24**, 4–10, https://doi.org/10.1130/GSATG214A.1.

Davis, C., B. Brown, and R. Bullock, 2006: Object-based verification of precipitation forecasts. Part I: Methodology and application to mesoscale rain areas. *Mon. Wea. Rev.*, **134**, 1772–1784, https://doi.org/10.1175/MWR3145.1.

Dietrich, W. E., R. Reiss, M.-L. Hsu, and D. R. Montgomery, 1995: A process-based model for colluvial soil depth and shallow landsliding using digital elevation data. *Hydrol. Processes*, **9**, 383–400, https://doi.org/10.1002/hyp.3360090311.

Elsaesser, G. S., and C. D. Kummerow, 2015: The sensitivity of rainfall estimation to error assumptions in a Bayesian passive microwave retrieval algorithm. *J. Appl. Meteor. Climatol.*, **54**, 408–422, https://doi.org/10.1175/JAMC-D-14-0105.1.

Emberson, R., D. Kirschbaum, P. Amatya, H. Tanyas, and O. Marc, 2022: Insights from the topographic characteristics of a large global catalog of rainfall-induced landslide event inventories. *Nat. Hazards Earth Syst. Sci.*, **22**, 1129–1149, https://doi.org/10.5194/nhess-22-1129-2022.

Farahmand, A., and A. AghaKouchak, 2013: A satellite-based global landslide model. *Nat. Hazards Earth Syst. Sci.*, **13**, 1259–1267, https://doi.org/10.5194/nhess-13-1259-2013.

Felsberg, A., G. J. M. D. Lannoy, M. Girotto, J. Poesen, R. H. Reichle, and T. Stanley, 2021: Global soil water estimates as landslide predictor: The effectiveness of SMOS, SMAP and GRACE observations, land surface simulations and data assimilation. *J. Hydrometeor.*, **22**, 1065–1084, https://doi.org/10.1175/JHM-D-20-0228.1.

Froude, M. J., and D. N. Petley, 2018: Global fatal landslide occurrence from 2004 to 2016. *Nat. Hazards Earth Syst. Sci.*, **18**, 2161–2181, https://doi.org/10.5194/nhess-18-2161-2018.

García-Delgado, H., S. Machuca, and E. Medina, 2019: Dynamic and geomorphic characterizations of the Mocoa debris flow (March 31, 2017, Putumayo Department, southern Colombia). *Landslides*, **16**, 597–609, https://doi.org/10.1007/s10346-018-01121-3.

Goodman, S. J., and Coauthors, 2013: The GOES-R Geostationary Lightning Mapper (GLM). *Atmos. Res.*, **125–126**, 34–49, https://doi.org/10.1016/j.atmosres.2013.01.006.

Guilloteau, C., R. Roca, and M. Gosset, 2016: A multiscale evaluation of the detection capabilities of high-resolution satellite precipitation products in West Africa. *J. Hydrometeor.*, **17**, 2041–2059, https://doi.org/10.1175/JHM-D-15-0148.1.

——, E. Foufoula-Georgiou, and C. D. Kummerow, 2017: Global multiscale evaluation of satellite passive microwave retrieval of precipitation during the TRMM and GPM Eras: Effective resolution and regional diagnostics for future algorithm development. *J. Hydrometeor.*, **18**, 3051–3070, https://doi.org/10.1175/JHM-D-17-0087.1.

——, ——, P. Kirstetter, J. Tan, and G. J. Huffman, 2021: How well do multisatellite products capture the space–time dynamics of precipitation? Part I: Five products assessed via a wavenumber–frequency decomposition. *J. Hydrometeor.*, **22**, 2805–2823, https://doi.org/10.1175/JHM-D-21-0075.1.

Guzzetti, F., S. Peruccacci, M. Rossi, and C. P. Stark, 2008: The rainfall intensity–duration control of shallow landslides and debris flows: An update. *Landslides*, **5**, 3–17, https://doi.org/10.1007/s10346-007-0112-1.

Han, S., and P. Coulibaly, 2017: Bayesian flood forecasting methods: A review. *J. Hydrol.*, **551**, 340–351, https://doi.org/10.1016/j.jhydrol.2017.06.004.

Harp, E. L., M. E. Reid, and J. A. Michael, 2004: Hazard analysis of landslides triggered by Typhoon Chata'an on July 2, 2002, in Chuuk State, Federated States of Micronesia. U.S. Geological Survey Open-File Rep. 2004-1348, 24 pp., https://doi.org/10.3133/ofr20041348.

Hartmann, J., and N. Moosdorf, 2012: The new global lithological map database GLiM: A representation of rock properties at the Earth surface. *Geochem. Geophys. Geosyst.*, **13**, Q12004, https://doi.org/10.1029/2012GC004370.

Hong, K. L., K.-L. Hsu, S. Sorooshian, and X. Gao, 2004: Precipitation estimation from remotely sensed imagery using an artificial neural network cloud classification system. *J. Appl. Meteor.*, **43**, 1834–1853, https://doi.org/10.1175/JAM2173.1.

Hong, Y., R. F. Adler, and G. Huffman, 2007: An experimental global prediction system for rainfall-triggered landslides using satellite remote sensing and geospatial datasets. *IEEE Trans. Geosci. Remote Sens.*, **45**, 1671–1680, https://doi.org/10.1109/TGRS.2006.888436.

Houze, R. A., Jr., 2012: Orographic effects on precipitating clouds. *Rev. Geophys.*, **50**, RG1001, https://doi.org/10.1029/2011RG000365.

Huang, M. Y.-F., and D. R. Montgomery, 2012: Fluvial response to rapid episodic erosion by earthquake and typhoons, Tachia River, central Taiwan. *Geomorphology*, **175–176**, 126–138, https://doi.org/10.1016/j.geomorph.2012.07.004.

Huffman, G. J., and Coauthors, 2007: The TRMM Multisatellite Precipitation Analysis (TMPA): Quasi-global, multiyear, combined-sensor precipitation estimates at fine scales. *J. Hydrometeor.*, **8**, 38–55, https://doi.org/10.1175/JHM560.1.

——, R. F. Adler, D. T. Bolvin, and E. J. Nelkin, 2010: The TRMM Multi-satellite Precipitation Analysis (TMPA). *Satellite Rainfall Applications for Surface Hydrology*, F. Hossain and M. Gebremichael, Eds., Springer, 3–22.

——, and Coauthors, 2019: Algorithm theoretical basis document (ATBD) version 5.2 for the NASA Global Precipitation Measurement (GPM) Integrated Multi-satellitE Retrievals for GPM (I-MERG). GPM Project Doc., 35 pp., https://gpm.nasa.gov/sites/default/files/document_files/IMERG_ATBD_V5.2.pdf.

Iida, T., 2004: Theoretical research on the relationship between return period of rainfall and shallow landslides. *Hydrol. Processes*, **18**, 739–756, https://doi.org/10.1002/hyp.1264.

Iverson, R. M., 2000: Landslide triggering by rain infiltration. *Water Resour. Res.*, **36**, 1897–1910, https://doi.org/10.1029/2000WR900090.

Jones, F. O., 1973: Landslides of Rio de Janeiro and the Serra das Araras escarpment, Brazil. USGS Professional Paper, 697, 49 pp., https://doi.org/10.3133/pp697.

Joyce, R. J., J. E. Janowiak, P. A. Arkin, and P. Xi, 2004: CMORPH: A method that produces global precipitation estimates from passive microwave and infrared data at high spatial and temporal resolution. *J. Hydrometeor.*, **5**, 487–503, https://doi.org/10.1175/1525-7541(2004)005<0487:CAMTPG>2.0.CO;2.

——, P. Xie, and J. E. Janowiak, 2011: Kalman filter–based CMORPH. *J. Hydrometeor.*, **12**, 1547–1563, https://doi.org/10.1175/JHM-D-11-022.1.

Kidd, C., T. Matsui, J. Chern, K. Mohr, C. D. Kummerow, and D. Randel, 2015: Precipitation estimates from cross-track passive microwave observations using a physically based retrieval scheme. *J. Hydrometeor.*, **17**, 383–400, https://doi.org/10.1175/JHM-D-15-0051.1.

——, J. Tan, P. Kirstetter, and W. A. Petersen, 2018: Validation of the version 05 level 2 precipitation products from the GPM Core Observatory and constellation satellite sensors. *Quart. J. Roy. Meteor. Soc.*, **144** (Suppl. 1), 313–328, https://doi.org/10.1002/qj.3175.

——, T. Matsui, and S. Ringerud, 2021a: Precipitation retrievals from passive microwave cross-track sensors: The precipitation retrieval and profiling scheme. *Remote Sens.*, **13**, 947, https://doi.org/10.3390/rs13050947.

——, G. Huffman, V. Maggioni, P. Chambon, and R. Oki, 2021b: The global satellite precipitation constellation: Current status and future requirements. *Bull. Amer. Meteor. Soc.*, **102**, E1844–E1861, https://doi.org/10.1175/BAMS-D-20-0299.1.

Kirschbaum, D., and T. Stanley, 2018: Satellite-based assessment of rainfall-triggered landslide hazard for situational awareness. *Earth's Future*, **6**, 505–523, https://doi.org/10.1002/2017EF000715.

——, R. Adler, Y. Hong, and A. Lerner-Lam, 2009: Evaluation of a preliminary satellite-based landslide hazard algorithm using global landslide inventories. *Nat. Hazards Earth Syst. Sci.*, **9**, 673–686, https://doi.org/10.5194/nhess-9-673-2009.

——, T. Stanley, and J. Simmons, 2015: A dynamic landslide hazard assessment system for Central America and Hispaniola. *Nat. Hazards Earth Syst. Sci.*, **15**, 2257–2272, https://doi.org/10.5194/nhess-15-2257-2015.

Kondo, K., S. Numamoto, and S. Hayashi, 2004: Disasters due to slope failures caused by Typhoon Meari (T0421) in Miyagawa village, Mie Prefecture. *J. Japan Landslide Soc.*, **41**, 419–422, https://doi.org/10.3313/jls.41.4_419.

Kotsuki, S., K. Kurosawa, S. Otsuka, K. Terasaki, and T. Miyoshi, 2019: Global precipitation forecasts by merging extrapolation-based nowcast and numerical weather prediction with locally optimized weights. *Wea. Forecasting*, **34**, 701–714, https://doi.org/10.1175/WAF-D-18-0164.1.

Kottek, M., J. Grieser, C. Beck, B. Rudolf, and F. Rubel, 2006: World Map of the Köppen-Geiger climate classification updated. *Meteor. Z.*, **15**, 259–263, https://doi.org/10.1127/0941-2948/2006/0130.

Kubota, T., and Coauthors, 2007: Global precipitation map using satellite-borne microwave radiometers by the GSMaP project: Production and validation. *IEEE Trans. Geosci. Remote Sens.*, **45**, 2259–2275, https://doi.org/10.1109/TGRS.2007.895337.

——, and Coauthors, 2020: Global Satellite Mapping of Precipitation (GSMaP) products in the GPM era. *Satellite Precipitation Measurement*, V. Levizzani et al., Eds., Advances in Global Change Research, Vol. 67, Springer, 355–373.

Kummerow, C. D., D. L. Randel, M. Kulie, N.-Y. Wang, R. Ferraro, S. Joseph Munchak, and V. Petkovic, 2015: The evolution of the Goddard profiling algorithm to a fully parametric scheme. *J. Atmos. Oceanic Technol.*, **32**, 2265–2280, https://doi.org/10.1175/JTECH-D-15-0039.1.

Lacerda, W. A., 1997: Stability of natural slopes along the tropical coast of Brazil. *Symp. on Recent Developments in Soil and Pavement Mechanics*, Rio de Janeiro, Brazil, Transportation Research Board, National Academy of Sciences, 17–39, https://trid.trb.org/view/476474.

Lin, G.-W., H. Chen, N. Hovius, M.-J. Horng, S. Dadson, P. Meunier, and M. Lines, 2008: Effects of earthquake and cyclone sequencing on landsliding and fluvial sediment transfer in a mountain catchment. *Earth Surf. Processes Landforms*, **33**, 1354–1373, https://doi.org/10.1002/esp.1716.

Mahrooghy, M., V. G. Anantharaj, N. H. Younan, W. A. Petersen, K.-L. Hsu, A. Behrangi, and J. Aanstoos, 2013: Augmenting satellite precipitation estimation with lightning information. *Int. J. Remote Sens.*, **34**, 5796–5811, https://doi.org/10.1080/01431161.2013.796100.

Marc, O., N. Hovius, P. Meunier, T. Uchida, and S. Hayashi, 2015: Transient changes of landslide rates after earthquakes. *Geology*, **43**, 883–886, https://doi.org/10.1130/G36961.1.

——, A. Stumpf, J.-P. Malet, M. Gosset, T. Uchida, and S.-H. Chiang, 2018: Initial insights from a global database of rainfall-induced landslide inventories: The weak influence of slope and strong influence of total storm rainfall. *Earth Surf. Dyn.*, **6**, 903–922, https://doi.org/10.5194/esurf-6-903-2018.

——, M. Gosset, H. Saito, T. Uchida, and J.-P. Malet, 2019: Spatial patterns of storm-induced landslides and their relation to rainfall anomaly maps. *Geophys. Res. Lett.*, **46**, 11 167–11 177, https://doi.org/10.1029/2019GL083173.

Marra, F., E. I. Nikolopoulos, E. N. Anagnostou, and E. Morin, 2018: Metastatistical extreme value analysis of hourly rainfall from short records: Estimation of high quantiles and impact of measurement errors. *Adv. Water Resour.*, **117**, 27–39, https://doi.org/10.1016/j.advwatres.2018.05.001.

——, M. Borga, and E. Morin, 2020: A unified framework for extreme subdaily precipitation frequency analyses based on ordinary events. *Geophys. Res. Lett.*, **47**, e2020GL090209, https://doi.org/10.1029/2020GL090209.

Mega, T., T. Ushio, M. Takahiro, T. Kubota, M. Kachi, and R. Oki, 2019: Gauge-adjusted global satellite mapping of precipitation. *IEEE Trans. Geosci. Remote Sens.*, **57**, 1928–1935, https://doi.org/10.1109/TGRS.2018.2870199.

Mehran, A., and A. AghaKouchak, 2014: Capabilities of satellite precipitation datasets to estimate heavy precipitation rates at different temporal accumulations. *Hydrol. Processes*, **28**, 2262–2270, https://doi.org/10.1002/hyp.9779.

Meunier, P., N. Hovius, and A. J. Haines, 2007: Regional patterns of earthquake-triggered landslides and their relation to ground motion. *Geophys. Res. Lett.*, **34**, L20408, https://doi.org/10.1029/2007GL031337.

Minjarez-Sosa, C. M., and J. Waissman, 2017: A survey and perspectives on mathematical models for quantitative precipitation estimation using lightning. *Adv. Meteor.*, **2017**, 1351308, https://doi.org/10.1155/2017/1351308.

Mirus, B. B., R. E. Becker, R. L. Baum, and J. B. Smith, 2018: Integrating real-time subsurface hydrologic monitoring with empirical rainfall thresholds to improve landslide early warning. *Landslides*, **15**, 1909–1919, https://doi.org/10.1007/s10346-018-0995-z.

Mondini, A. C., 2017: Measures of spatial autocorrelation changes in multitemporal SAR images for event landslides detection. *Remote Sens.*, **9**, 554, https://doi.org/10.3390/rs9060554.

Netto, A. L. C., and Coauthors, 2013: January 2011: The extreme landslide disaster in Brazil. *Landslide Science and Practice*, Springer, 377–384.

Nikolopoulos, E. I., E. Destro, V. Maggioni, F. Marra, and M. Borga, 2017: Satellite rainfall estimates for debris flow prediction: An evaluation based on rainfall accumulation–duration thresholds. *J. Hydrometeor.*, **18**, 2207–2214, https://doi.org/10.1175/JHM-D-17-0052.1.

Oliveira, R., V. Maggioni, D. Vila, and C. Morales, 2016: Characteristics and diurnal cycle of GPM rainfall estimates over the central Amazon region. *Remote Sens.*, **8**, 544, https://doi.org/10.3390/rs8070544.

Otsuka, S., S. Kotsuki, and T. Miyoshi, 2016: Nowcasting with data assimilation: A case of global satellite mapping of precipitation. *Wea. Forecasting*, **31**, 1409–1416, https://doi.org/10.1175/WAF-D-16-0039.1.

Ozturk, U., H. Saito, Y. Matsushi, I. Crisologo, and W. Schwanghart, 2021: Can global rainfall estimates (satellite and reanalysis) aid landslide hindcasting? *Landslides*, **18**, 3119–3133, https://doi.org/10.1007/s10346-021-01689-3.

Petley, D., 2012: Global patterns of loss of life from landslides. *Geology*, **40**, 927–930, https://doi.org/10.1130/G33217.1.

Piepgrass, M. V., E. P. Krider, and C. B. Moore, 1982: Lightning and surface rainfall during Florida thunderstorms. *J. Geophys. Res.*, **87**, 11 193–11 201, https://doi.org/10.1029/JC087iC13p11193.

Prancevic, J. P., M. P. Lamb, B. W. McArdell, C. Rickli, and J. W. Kirchner, 2020: Decreasing landslide erosion on steeper slopes in soil-mantled landscapes. *Geophys. Res. Lett.*, **47**, e2020GL087505, https://doi.org/10.1029/2020GL087505.

Reiser, H., and H. Kutiel, 2009: Rainfall uncertainty in the Mediterranean: Definitions of the daily rainfall threshold (DRT) and the rainy season length (RSL). *Theor. Appl. Climatol.*, **97**, 151–162, https://doi.org/10.1007/s00704-008-0055-z.

Roberts, N. M., and H. W. Lean, 2008: Scale-selective verification of rainfall accumulations from high-resolution forecasts of convective events. *Mon. Wea. Rev.*, **136**, 78–97, https://doi.org/10.1175/2007MWR2123.1.

Roca, R., P. Chambon, I. Jobard, P. E. Kirstetter, M. Gosset, and J. C. Bergès, 2010: Comparing satellite and surface rainfall products over West Africa at meteorologically relevant scales during the AMMA campaign using error estimates. *J. Appl. Meteor. Climatol.*, **49**, 715–731, https://doi.org/10.1175/2009JAMC2318.1.

Rossi, M., S. Luciani, D. Valigi, D. Kirschbaum, M. T. Brunetti, S. Peruccacci, and F. Guzzetti, 2017: Statistical approaches for the definition of landslide rainfall thresholds and their uncertainty using rain gauge and satellite data. *Geomorphology*, **285**, 16–27, https://doi.org/10.1016/j.geomorph.2017.02.001.

Rosso, R., M. C. Rulli, and G. Vannucchi, 2006: A physically based model for the hydrologic control on shallow landsliding.

Water Resour. Res., **42**, W06410, https://doi.org/10.1029/2005WR004369.

Saito, H., and H. Matsuyama, 2012: Catastrophic landslide disasters triggered by record-breaking rainfall in Japan: Their accurate detection with normalized soil water index in the Kii Peninsula for the year 2011. *SOLA*, **8**, 81–84, https://doi.org/10.2151/sola.2012-021.

——, and ——, 2015: Probable hourly precipitation and soil water index for 50-yr recurrence interval over the Japanese archipelago. *SOLA*, **11**, 118–123, https://doi.org/10.2151/sola.2015-028.

——, O. Korup, T. Uchida, S. Hayashi, and T. Oguchi, 2014: Rainfall conditions, typhoon frequency, and contemporary landslide erosion in Japan. *Geology*, **42**, 999–1002, https://doi.org/10.1130/G35680.1.

Schultz, C. J., W. A. Petersen, and L. D. Carey, 2011: Lightning and severe weather: A comparison between total and cloud-to-ground lightning trends. *Wea. Forecasting*, **26**, 744–755, https://doi.org/10.1175/WAF-D-10-05026.1.

Shige, S., S. Kida, H. Ashiwake, T. Kubota, and K. Aonashi, 2013: Improvement of TMI rain retrievals in mountainous areas. *J. Appl. Meteor. Climatol.*, **52**, 242–254, https://doi.org/10.1175/JAMC-D-12-074.1.

Shuin, Y., N. Hotta, M. Suzuki, and K. Ogawa, 2012: Estimating the effects of heavy rainfall conditions on shallow landslides using a distributed landslide conceptual model. *Phys. Chem. Earth*, **49**, 44–51, https://doi.org/10.1016/j.pce.2011.06.002.

Soula, S., and S. Chauzy, 2001: Some aspects of the correlation between lightning and rain activities in thunderstorms. *Atmos. Res.*, **56**, 355–373, https://doi.org/10.1016/S0169-8095(00)00086-7.

Stanley, T. A., D. B. Kirschbaum, G. Benz, R. A. Emberson, P. M. Amatya, W. Medwedeff, and M. K. Clark, 2021: Data-driven landslide nowcasting at the global scale. *Front. Earth Sci.*, **9**, 9, 640043, https://doi.org/10.3389/feart.2021.640043.

Stumpf, A., N. Lachiche, J.-P. Malet, N. Kerle, and A. Puissant, 2014: Active learning in the spatial domain for remote sensing image classification. *IEEE Trans. Geosci. Remote Sens.*, **52**, 2492–2507, https://doi.org/10.1109/TGRS.2013.2262052.

Tan, J., W. A. Petersen, and A. Tokay, 2016: A novel approach to identify sources of errors in IMERG for GPM ground validation. *J. Hydrometeor.*, **17**, 2477–2491, https://doi.org/10.1175/JHM-D-16-0079.1.

——, ——, G. Kirchengast, D. C. Goodrich, and D. B. Wolff, 2018: Evaluation of Global Precipitation Measurement rainfall estimates against three dense gauge networks. *J. Hydrometeor.*, **19**, 517–532, https://doi.org/10.1175/JHM-D-17-0174.1.

——, G. J. Huffman, D. T. Bolvin, E. J. Nelkin, and M. Rajagopal, 2021: SHARPEN: A scheme to restore the distribution of averaged precipitation fields. *J. Hydrometeor.*, **22**, 2105–2116, https://doi.org/10.1175/JHM-D-20-0225.1.

Taniguchi, A., and Coauthors, 2013: Improvement of high-resolution satellite rainfall product for Typhoon Morakot (2009) over Taiwan. *J. Hydrometeor.*, **14**, 1859–1871, https://doi.org/10.1175/JHM-D-13-047.1.

Terzaghi, K., 1943: Effect of seepage on the conditions for equilibrium in ideal sand. *Theoretical Soil Mechanics*, John Wiley and Sons, 235–264.

Thomas, M. A., B. B. Mirus, and B. D. Collins, 2018: Identifying physics-based thresholds for rainfall-induced landsliding. *Geophys. Res. Lett.*, **45**, 9651–9661, https://doi.org/10.1029/2018GL079662.

——, B. D. Collins, and B. B. Mirus, 2019: Assessing the feasibility of satellite-based thresholds for hydrologically driven landsliding. *Water Resour. Res.*, **55**, 9006–9023, https://doi.org/10.1029/2019WR025577.

Turk, F. J., and Coauthors, 2021: Adapting passive microwave-based precipitation algorithms to variable microwave land surface emissivity to improve precipitation estimation from the GPM constellation. *J. Hydrometeor.*, **22**, 1755–1781, https://doi.org/10.1175/JHM-D-20-0296.1.

UNOSAT, 2016: Landslide affected areas in southeastern Dominica. accessed 27 June 2022, https://unitar.org/maps/map/2281.

Ushio, T., and Coauthors, 2009: A Kalman filter approach to the Global Satellite Mapping of Precipitation (GSMaP) from combined passive microwave and infrared radiometric data. *J. Meteor. Soc. Japan*, **87A**, 137–151, https://doi.org/10.2151/jmsj.87A.137.

van Asch, T. W. J., J. Buma, and L. P. H. Van Beek, 1999: A view on some hydrological triggering systems in landslides. *Geomorphology*, **30**, 25–32, https://doi.org/10.1016/S0169-555X(99)00042-2.

van Westen, C. J., and J. Zhang, 2018: Tropical Cyclone Maria. Inventory of landslides and flooded areas. UNITAR-UNOSAT, accessed 27 June 2022, http://www.unitar.org/unosat/node/44/2762.

von Ruette, J., P. Lehmann, and D. Or, 2014: Effects of rainfall spatial variability and intermittency on shallow landslide triggering patterns at a catchment scale. *Water Resour. Res.*, **50**, 7780–7799, https://doi.org/10.1002/2013WR015122.

Wang, F., Y.-H. Wu, H. Yang, Y. Tanida, and A. Kamei, 2015: Preliminary investigation of the 20 August 2014 debris flows triggered by a severe rainstorm in Hiroshima City, Japan. *Geoenviron. Disasters*, **2**, 17, https://doi.org/10.1186/s40677-015-0025-6.

Wang, G., A. Suemine, G. Furuya, M. Kaibori, and K. Sassa, 2005: Rainstorm-induced landslides at Kisawa village, Tokushima Prefecture, Japan, August 2004. *Landslides*, **2**, 235–242, https://doi.org/10.1007/s10346-005-0061-5.

Watakabe, T., and Y. Matsushi, 2019: Lithological controls on hydrological processes that trigger shallow landslides: Observations from granite and hornfels hillslopes in Hiroshima, Japan. *Catena*, **180**, 55–68, https://doi.org/10.1016/j.catena.2019.04.010.

Wilson, R. C., and G. F. Wieczorek, 1995: Rainfall thresholds for the initiation of debris flows at La Honda, California. *Environ. Eng. Geosci.*, **I**, 11–27, https://doi.org/10.2113/gseegeosci.I.1.11.

Wu, W., R. Emerton, Q. Duan, A. W. Wood, F. Wetterhall, and D. E. Robertson, 2020: Ensemble flood forecasting: Current status and future opportunities. *Wiley Interdiscip. Rev.: Water*, **7**, e1432, https://doi.org/10.1002/wat2.1432.

Xu, W., R. F. Adler, and N.-Y. Wang, 2013: Improving geostationary satellite rainfall estimates using lightning observations: Underlying lightning–rainfall–cloud relationships. *J. Appl. Meteor. Climatol.*, **52**, 213–229, https://doi.org/10.1175/JAMC-D-12-040.1.

Yamamoto, M. K., S. Shige, C.-K. Yu, and L.-W. Cheng, 2017: Further improvement of the heavy orographic rainfall retrievals in the GSMaP algorithm for microwave radiometers. *J. Appl. Meteor. Climatol.*, **56**, 2607–2619, https://doi.org/10.1175/JAMC-D-16-0332.1.

You, Y., and Coauthors, 2020a: Comparison of TRMM microwave imager rainfall datasets from NASA and JAXA. *J. Hydrometeor.*, **21**, 377–397, https://doi.org/10.1175/JHM-D-19-0022.1.

——, V. Petkovic, J. Tan, R. Kroodsma, W. Berg, C. Kidd, and C. Peters-Lidard, 2020b: Evaluation of V05 precipitation estimates from GPM constellation radiometers using KuPR as the reference. *J. Hydrometeor.*, **21**, 705–728, https://doi.org/10.1175/JHM-D-19-0144.1.

Zorzetto, E., G. Botter, and M. Marani, 2016: On the emergence of rainfall extremes from ordinary events. *Geophys. Res. Lett.*, **43**, 8076–8082, https://doi.org/10.1002/2016GL069445.